Contrib Mineral Petrol (2013) 165:981–1008
DOI 10.1007/s00410-012-0844-3

ORIGINAL PAPER

Major and trace-element composition and pressure–temperature evolution of rock-buffered fluids in low-grade accretionary-wedge metasediments, Central Alps

George D. Miron · Thomas Wagner ·
Markus Wälle · Christoph A. Heinrich

Received: 22 January 2012 / Accepted: 18 October 2012 / Published online: 28 December 2012

Abstract The chemical composition of fluid inclusions in quartz crystals from Alpine fissure veins was determined by combination of microthermometry, Raman spectroscopy, and LA-ICPMS analysis. The veins are hosted in carbonate-bearing, organic-rich, low-grade metamorphic metapelites of the Bündnerschiefer of the eastern Central Alps (Switzerland). This strongly deformed tectonic unit is interpreted as a partly subducted accretionary wedge, on the basis of widespread carpholite assemblages that were later overprinted by lower greenschist facies metamorphism. Veins and their host rocks from two locations were studied to compare several indicators for the conditions during metamorphism, including illite crystallinity, graphite thermometry, stability of mineral assemblages, chlorite thermometry, fluid inclusion solute thermometry, and fluid inclusion isochores. Fluid inclusions are aqueous two-phase with 3.7–4.0 wt% equivalent NaCl at Thusis and 1.6–1.7 wt% at Schiers. Reproducible concentrations of Li, Na, K, Rb, Cs, Mg, Ca, Sr, Ba, B, Al, Mn, Cu, Zn, Pb, As, Sb, Cl, Br, and S could be determined for 97 fluid inclusion assemblages. Fluid and mineral geothermometry consistently indicate temperatures of 320 ± 20 °C for the host rocks at Thusis and of 250 ± 30 °C at Schiers. Combining fluid inclusion isochores with independent geothermometers results in pressure estimates of 2.8–3.8 kbar for Thusis, and of 3.3–3.4 kbar for Schiers. Pressure–temperature estimates are confirmed by pseudosection modeling. Fluid compositions and petrological modeling consistently demonstrate that chemical fluid-rock equilibrium was attained during vein formation, indicating that the fluids originated locally by metamorphic dehydration during near-isothermal decompression in a rock-buffered system.

Keywords Fluid inclusions · LA-ICPMS · Low-grade metamorphism · Accretionary wedge · Veins · Fluid-rock equilibrium · Graphitic metasediments

Introduction

The chemical composition of metamorphic fluids is of fundamental importance for predicting mineral stability, evaluating the pressure–temperature history of rocks, and assessing rates and scales of mass transfer during fluid flow in subduction zones and compressional orogens. Investigation of the fluid evolution in accretionary wedges is of particular geodynamic interest for understanding element mobility during subduction and partial return of sedimentary and hydrous upper-crustal material to the mantle (Saffer and Tobin 2011). The Bündnerschiefer (Schistes Lustrés) units occurring throughout the Western, Central, and parts of the Eastern Alps represent the sedimentary part of an accretionary-wedge complex, formed during subduction of the Alpine Tethys and eventual collision of the Adriatic plate and smaller continental blocks with the European continent (Laubscher and Bernoulli 1982;

Communicated by T. L. Grove.

Electronic supplementary material The online version of this article (doi:10.1007/s00410-012-0844-3) contains supplementary material, which is available to authorized users.

G. D. Miron (✉) · T. Wagner · M. Wälle · C. A. Heinrich
Institute of Geochemistry and Petrology, ETH Zurich,
Clausiusstrasse 25, 8092 Zurich, Switzerland
e-mail: mirondanro@yahoo.com

T. Wagner
Department of Geosciences and Geography,
University of Helsinki, P.O.Box 64 (Gustaf Hällströmin katu 2a),
00014 Helsinki, Finland

Oberhänsli et al. 1995; Schmid et al. 1996; Bousquet et al. 1998; Stampfli et al. 1998; Wiederkehr et al. 2008, 2009). Due to extensive studies of the resulting nappe structure and the polyphase metamorphic history of the Alpine orogen (Niggli and Niggli 1965; Trommsdorff 1966; Frey and Ferreiro Mählmann 1999), these lithologically rather monotonous dark calcareous shales and siltstones provide an excellent natural laboratory for studying the evolution of metamorphic fluids related to partial subduction and subsequent uplift and incorporation of sedimentary material into continental collision zones.

Commonly in petrology, the properties of metamorphic fluids are inferred from mineral paragenesis using equilibrium thermodynamic calculations, which largely ignore the effect of dissolved salts or of major mass transfer except for H_2O and CO_2 (Thompson 2010). Fluid composition with regard to minor dissolved components can be predicted from fluid-rock equilibrium, assuming that the fluid composition was controlled by mineral solubilities, and that little external fluid has infiltrated the rocks. However, many field-based studies, including observations of widespread veins in metasedimentary rocks, show that fluid migration is ubiquitous during metamorphism (Brantley and Voigt 1989; Manning 2004). These observations imply that rocks adjust their mineralogy to attain equilibrium with fluids passing through them (Oliver and Bons 2001; Thompson 1997, 2010) and may thereby change their bulk composition, notably with regard to minor volatile components and ore forming elements (Ague 1994, 2003). Bulk-compositional studies of Bündnerschiefer metasediments (Garofalo 2011) did not show evidence for systematic large-scale mobilization of chemical elements with possible exception of B and Li, but primary compositional variations may obscure significant mass transfer. Under low-grade metamorphic conditions, mineral reactions frequently do not reach equilibrium, making it even more difficult to characterize metamorphic conditions and assess mass transfer by fluids from thermodynamic calculations alone (Árkai et al. 2000, 2002; Merriman and Peacor 1999; Miron et al. 2012).

Fluid inclusions can provide direct information about fluid composition as well as pressure and temperature of metamorphism (Touret 2001). The Alps have long been known for metamorphic veins with large euhedral crystals, mainly quartz (Poty et al. 1974; Mullis 1975, 1979; Mullis et al. 1994). These quartz crystals contain abundant assemblages of large and well-preserved fluid inclusions that were shown to be closely related to the metamorphic history of the surrounding rocks (Poty et al. 1974; Mullis 1975, 1987, 1988, 1996; Frey et al. 1980; Mullis et al. 1994; Agard et al. 2000; Tarantola et al. 2007). Fluid inclusion characteristics were determined using microthermometry, Raman spectroscopy, chemical, and stable isotope analysis involving bulk crush-leach methods (e.g., K/Na analysis; Yardley et al. 1993; Mullis et al. 1994; McCaig et al. 2000). Poty et al. (1974) and Mullis et al. (1994) showed a systematic compositional distribution of fluid populations in veins of the Central Alps, based on careful establishment of fluid inclusion and quartz growth chronology. The composition of the earliest fluid inclusion populations changes systematically with increasing metamorphic grade of the local host rocks, from the diagenetic zone to amphibolites-facies conditions, whereby accompanying vein minerals closely reflect the composition of the local host rock (Mazurek 1999; Mullis et al. 1994, 2002; Tarantola et al. 2007, 2009).

This study reports the first detailed dataset of the chemical composition of metamorphic fluids, including major and minor rock-forming elements, important ligands, and selected trace ore metals, from quartz veins hosted in metasediments of the Bündnerschiefer (Swiss Alps), determined by quantitative LA-ICPMS microanalysis of petrographically controlled fluid inclusion generations. The data provide direct insight into fluid-rock equilibria, transport of trace metals and volatile elements by metamorphic fluids, the source signature of the fluids (e.g., Br/Cl ratios), and the nature of dehydration processes in organic-rich metapelites that were partly subducted in an accretionary wedge. Fluid compositions are linked with the pressure–temperature conditions of the host rocks that are reconstructed from conventional geothermobarometry and pseudosection modeling. Entrapment temperatures of the fluids are independently calculated from several solute geothermometers and used to evaluate the attainment of fluid-rock equilibrium. The pressure–temperature paths reconstructed for the veins and their host rocks finally provide constraints for the thermal and geodynamic history of the Bündnerschiefer accretionary-wedge complex.

Regional geology

The studied locations are situated in the North Penninic Bündnerschiefer enveloping and pushed ahead of the Penninic basement nappes (Fig. 1). They are tectonically intercalated between the Helvetic units below (basement massifs and shelf sediment cover of the European continent) and the Middle Penninic, South Penninic nappes, and the Austroalpine thrust sheet, representing the Adriatic plate that did not experience significant Alpine metamorphism (e.g., Steinmann 1994). The Bündnerschiefer rocks share many features with the Schistes Lustrés in the Western Alps (Steinmann 1994) and are viewed as representing an accretionary prism associated with the subduction of two oceanic basins between Europe and Adria-Africa (Oberhänsli et al. 1995; Bousquet et al. 1998; Wiederkehr et al. 2008, 2009). The Bündnerschiefer consists of very low to low-grade metamorphic shaly-calcareous-sandy sedimentary rocks (mainly dark, fine-grained mudstones with varying amounts of sandstones, limestones, and organic matter). Most of the rocks are of deep oceanic facies (Cretaceous) followed by flysch formations (Late Cretaceous to Eocene) of a shallow oceanic facies (Steinmann 1994). The metamorphic grade increases from N to S and from ENE to WSW, ranging from higher diagenesis to lower amphibolites facies conditions (Ferreiro Mählmann et al. 2002). Locally, relicts of high-pressure low-temperature metamorphism are preserved, which are overprinted by greenschist facies metamorphism (Bousquet et al. 1998).

The first metamorphic event occurred during the closure of the North Penninic Ocean, commencing in the Paleocene and being contemporaneous with the paleocene-eocene eclogite formation in the Adula nappe (Oberhänsli et al. 1995). Omphacite-quartz-garnet assemblages occur in typical Bündnerschiefer rocks that are immediately attached to and envelope the Adula nappe near Vals (Heinrich 1986), demonstrating that regional blueschist to eclogite facies metamorphism is of Alpine age. The first high-pressure low-temperature (HP/LT) phase in the Bündnerschiefer further north is related to subduction and sediment accretion which lead to the formation of minerals typical for subduction under HP/LT conditions such as carpholite and lawsonite (Oberhänsli et al. 1995; Agard et al. 2000; Bousquet et al. 2002; Wiederkehr et al. 2008,

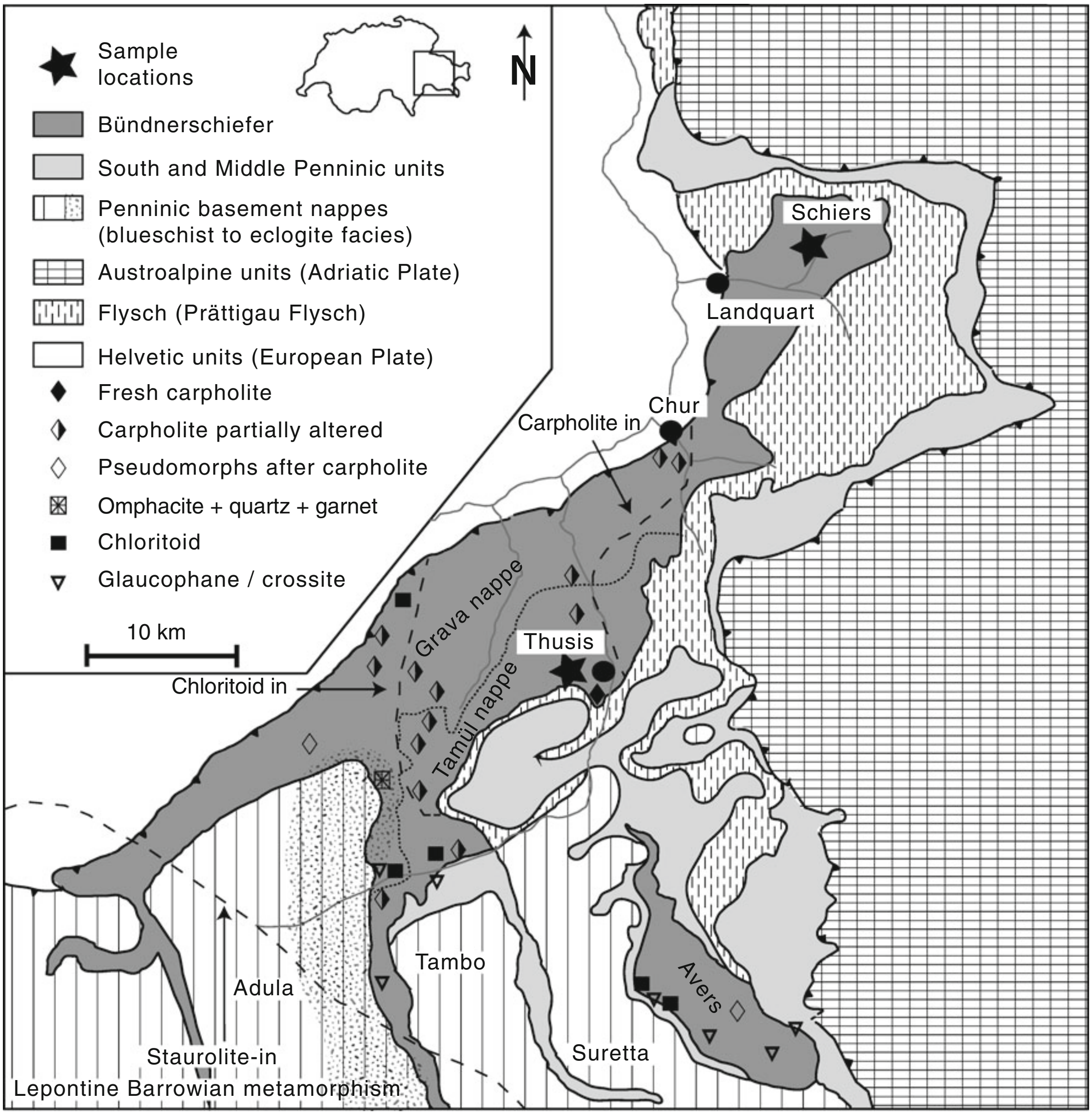

Fig. 1 Map illustrating the regional geology and sample locations. Redrawn from Ferreiro Mählmann et al. (2002), with the occurrence of indicator minerals and isograds adapted from Oberhänsli et al. (1995) and Frey and Ferreiro Mählmann (1999). The occurrence of carpholite is indicative of the high-pressure metamorphic stage

2009). During the subduction process and subsequent syncollisional exhumation, deeper parts of the wedge were transported above lower-pressure units, resulting in an almost isothermal decompression (early oligocene; Wiederkehr et al. 2009). The exhumation is associated with the breakdown of Fe–Mg carpholite (Wiederkehr et al. 2009) and lawsonite (Agard et al. 2000) to muscovite-chlorite-clinozoisite/epidote-quartz assemblages of a greenschist facies overprint (Wiederkehr et al. 2009; Oberhänsli et al. 1995; Bousquet et al. 2002). This lower-pressure medium-temperature (LP/MT) Barrovian metamorphic event outlasted continent–continent collision, resulting in mineral isograds that crosscut major nappe boundaries (e.g., staurolite isograd in dolmitic lithologies; Trommsdorff 1966; Frey and Ferreiro Mählmann 1999; Fig. 1).

The rocks in the study area are composed of a sheet silicate assemblage of illite, chlorite, mixed-layer paragonite-phengite and paragonite, with chloritoid occurring in the greenschist facies rocks (Frey 1974). Although albite is sometimes present, the feldspar-absent paragonite-calcite and paragonite-dolomite assemblages are more common, with paragonite being the essential Na-bearing phase (Frey 1974, 1986, 1987a, 1988). Metamorphic temperature–pressure conditions during the first event were estimated at 350 °C and 7 kbar close to Chur, and at 400 °C and 14 kbar in the area W of Thusis. These conditions indicate a low-temperature blueschist metamorphic event (low-pressure and -temperature for Chur), which was mostly overprinted by greenschist facies metamorphism (Oberhänsli et al. 1995; Frey and Ferreiro Mählmann 1999; Ferreiro Mählmann et al. 2002).

Field geology

Quartz veins and related wall- and host-rock samples were collected from two locations in the Bündnerschiefer, which cover the transition from very low to low-grade metamorphic conditions (Oberhänsli et al. 1995; Frey and Ferreiro Mählmann 1999; Ferreiro Mählmann et al. 2002). One place is located near the village of Thusis, the second one north of Chur, close to the village of Schiers (Fig. 1). Further on these two places will be referred to as Thusis and Schiers.

The Bündnerschiefer rocks around Thusis contain at least two generations of quartz veins hosted by variably carbonate-bearing organic matter rich metapelites and fine-grained feldspathic graywackes (Figs. 2, 3). A first generation of veins is very abundant, making up about 5 % of the rock volume in most outcrops. They are essentially parallel to the main foliation (strike: 030°, dip: 20–45° SE), and are partly deformed conforming to the same sense of shear that is observed during development of the main foliation. The length of these veins varies between 10 cm and 1 m and they have a thickness of 10–20 cm (Fig. 2a). These veins are characterized by a massive texture of coarse-grained quartz and calcite as the vein filling, whereas chlorite is conspicuously absent (Fig. 2b). The second vein generation is sigmoidal gash-type fissure veins with open crystal filled vugs and cavities, which are less abundant than the foliation-parallel veins (Fig. 2c). They crosscut the main foliation at high angles, have an almost N–S orientation (strike: about 170°), and probably developed parallel to the maximum principal stress at an angle of about 45° to the shear plane (Goscombe et al. 2004). They can be larger than the foliation-parallel veins and reach up to 1–2 m in length and a thickness in the central part of up to a meter. A typical feature is their sigmoidal shape and the presence of different generations of well-crystallized euhedral minerals protruding into open space, including mainly quartz, calcite, and chlorite (Fig. 2d). The overall vein shape and the complex growth features of free-standing and commonly isolated quartz crystals show that crystallization occurred during repeated brittle failure of the vein material while vein opening and ductile deformation proceeded in the host metasediments.

The Bündnerschiefer in the area of Schiers hosts two vein generations in carbonate-rich metapelites with similar orientation as those in the area of Thusis, one being foliation parallel and a second one that intersects the foliation at high angles. Both vein generations show clear indication of brittle deformation, the quartz being extensively fractured. The foliation-parallel veins are very abundant, have lengths of 10 cm to 1 m, and a thickness between 10 and 20 cm. The open-fissure veins that crosscut the foliation are larger than the foliation-parallel veins, with lengths between 50 cm to about 1.5 m and thicknesses from 20 cm to 1 m. Only smaller vugs have remained open, different form the large volume of open space that is typically present in the veins in the Thusis area. There is no mineralogical difference between the two sets of veins, and both contain quartz and carbonates as the major vein filling.

Samples and methods

Representative samples of veins, wall rocks adjacent to the veins (less than 40 cm from the vein contact), and host rocks were investigated from both localities (Table 1). Samples at Thusis were collected from the wall- and host rock at different distances from the open-fissure veins, in order to identify possible hydrothermal alteration effects and to obtain a complete chemical and mineralogical dataset that could be used to constrain phase equilibria computation (Fig. 3). Foliation-parallel veins and their adjacent wall rock were sampled at several meters distance from the open-fissure veins. Samples of the open-fissure veins were taken from the elongate-

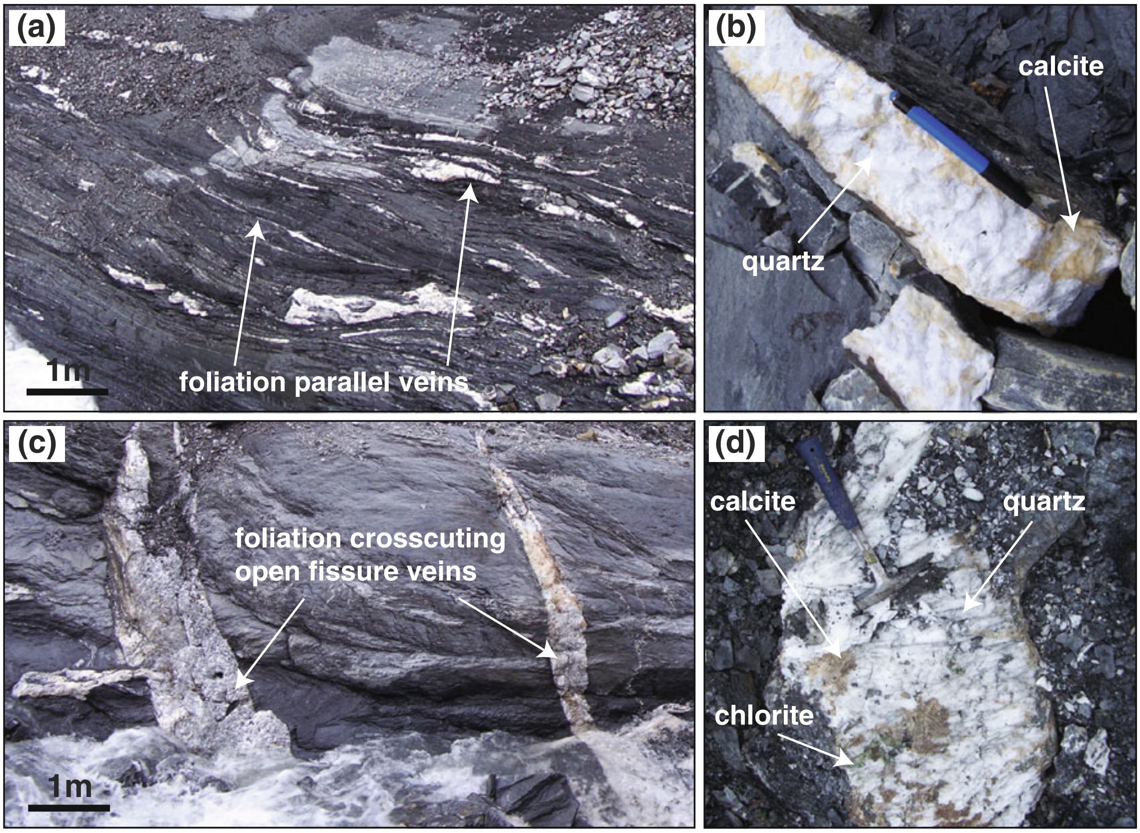

Fig. 2 Photographs illustrating the field and structural relationships of the two principal vein types from Thusis. **a** Foliation-parallel veins in the metapelitic host rocks. **b** Detail of a foliation-parallel vein. Coarse-grained quartz is intergrown with Fe-bearing calcite. **c** Example of a set of open-fissure veins intersecting the main foliation at high angle. **d** Detail of an open-fissure vein. The marginal zone is composed of elongate-blocky quartz, calcite, and minor chlorite, and the central zone contains euhedral quartz crystals

blocky quartz close to the wall rock and from the euhedral quartz crystals present in the central part of the veins. Samples from Schiers included material from the two vein generations as well as representative wall- and host rocks. Wall- and host-rock samples from both localities were used for whole-rock chemical analysis, XRD, and illite crystallinity determination, and material from the two generations of quartz veins was used for fluid inclusion studies. Fluid inclusion types, assemblages, and their relative chronology were established by detailed fluid inclusion petrography. The fluid inclusion studies were based on consequent application of the concept of fluid inclusion assemblages (FIA) (Goldstein and Reynolds 1994), that is, groups of fluid inclusions that were trapped together on temporally constrained growth features (growth zones, single healed fractures). Fluid inclusion assemblages are equivalent to groups of synchronous inclusions (GIS; Touret 2001).

Raman spectroscopy

Raman spectra of rock and fluid inclusion samples were analyzed using a LabRam HR instrument from Horiba, equipped with a 633-nm (12 mW source) laser. The spectrometer was calibrated using a silicon standard. For fluid inclusions, the instrument settings and methods were adopted from Burke (2001; for review see Frezzotti et al. 2012). Slabs of rock samples were used to analyze the carbonaceous material (CM). The Raman spectra of carbonaceous material can be affected by different analytical settings, and the procedure described by Beyssac et al. (2002, 2003) and Aoya et al. (2010) was used. The spectra are composed of a graphitic band (G) around 1,580–1,600 cm^{-1}, corresponding to the ideal graphite lattice vibration, and a composite defect band (D), composed of several defect bands characteristic for disordered graphite, at frequencies between 1,100 and 1,800 cm^{-1}. Ten to twenty spectra were recorded from each slab, and the peak area of the Raman bands was then obtained by fitting the spectra with the Peak Fit v. 4.12 software. Calibration for geothermometry was done with both a 514- and 532-nm laser (Aoya et al. 2010; Beyssac et al. 2002). Because graphite defect bands are dispersive, their positions and relative area vary with the incident laser wavelength (Pimenta et al. 2007). Aoya et al. (2010) compared the influence of using different laser wavelengths and

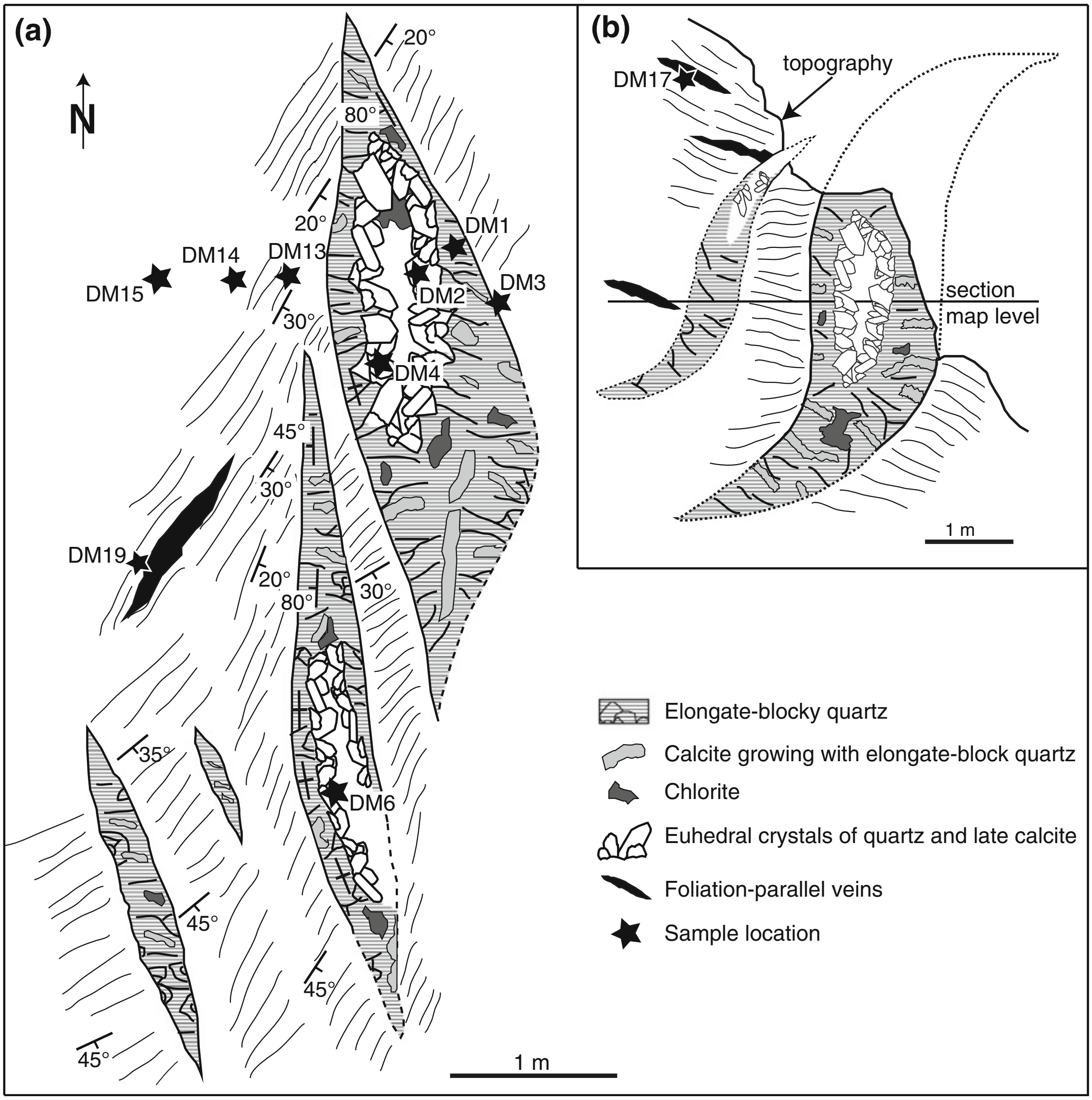

Fig. 3 Field sketches illustrating the structure, mineralogy, and filling sequence of the open-fissure veins that were mapped and sampled in the Thusis area. **a** Map view of the vein exposure, with structural data and sample locations. **b** Cross-section view of the open-fissure vein, illustrating relations to the foliation-parallel veins. The *horizontal line* represents the level of the map view

concluded that for highly disordered carbonaceous material (samples with R2 of 0.5–0.7; R2 = D1/(G + D1 + D2), and R1 = D1/G, where G, D1, D2 are the CM Raman bands; Sadezky et al. 2005), the wavelength dependence of the Raman spectrum of CM appears to be negligible, corresponding to an error in temperature determination of 5 °C (Aoya et al. 2010). Temperature was calculated using the integrated peak areas using the equations of Beyssac et al. (2002) and Aoya et al. (2010).

X-ray powder diffraction

Textured, air dried, < 2 μm fractions of host-rock samples were analyzed at the University of Lausanne to determine the Kübler index (KI) and Árkai index (AI). The KI represents the full width at half maximum (FWHM) in $\Delta°2\theta$ for (001) basal reflection of illite/muscovite and the AI the FWHM in $\Delta°2\theta$ for (001) and (002) basal reflections of chlorite. Sample preparation and instrument settings were the same as described previously (Kisch 1991; Árkai et al. 2000). Powdered whole-rock samples were analyzed using a Bruker AXS D8 Advance X-ray diffractometer (K-α radiation, 40 kV, 30 mA) for qualitative and quantitative mineral determination. The program EVA 3.0 (Bruker AXS) was used for identifying the mineral phases in the XRD pattern. The quantification was based on a Rietveld method using the AutoQuan software package.

Table 1 List of investigated samples (wall rock and quartz veins), summary description, Árkai index (AI), Kübler index (KI), and mineral abundance determined by XRD

Sample	Description	AI	AI	KI	Mineral abundance from XRD (vol%)								
		001*	002*	001*	qtz	chl	ms	pg	czo	cal	ank	rt	ab
Thusis													
DM3	Vein-wall-rock contact, fine-grained shale	0.20	0.19	0.25									
DM13	Metapelite, 15 cm	0.20	0.19	0.23	33	30	29	5	n.d.	n.d.	1	2	n.d.
DM14	Metapelite, 30 cm	0.21	0.19	0.24	18	35	33	10	2	1	n.d.	1	n.d.
DM15	Metapelite, 1 m	0.18	0.18	0.25	43	20	28	4	n.d.	1	3	1	n.d.
DM16	Metapelite, 5 m	0.20	0.19	0.22	27	32	29	5	2	1	n.d.	1	3
DM17	Vein-wall-rock pair of foliation-parallel quartz vein	0.19	0.18	0.22									
DM18	Metapelite, 5 m	0.20	0.19	0.24	27	21	33	16	1	1	n.d.	1	n.d.
DM19	Vein-wall-rock pair of foliation-parallel quartz vein	0.19	0.18	0.22	19	38	25	16	n.d.	n.d.	1	1	n.d.
DM24	Metapelite, 50 m	0.20	0.19	0.21									
DM17qtz	Elongate-blocky quartz crystal from foliation-parallel vein (FI assemblages A)												
DM1qtz	Elongate-blocky quartz from open-fissure vein (FI assemblages B)												
DM2qtz	10 cm euhedral quartz crystal from open-fissure vein (FI assemblages C)												
DM4qtz	4 cm euhedral quartz crystal from open-fissure vein (FI assemblages D)												
DM6qtz	4 cm euhedral quartz crystal from open-fissure vein (FI assemblages E)												
Schiers													
DM30	Very fine-grained carbonate-rich shale	0.17	0.19	0.28	22	7	17	n.d.	n.d.	53	n.d.	1	n.d.
DM38	Vein-wall-rock pair, open-fissure vein with adjacent wall rock (very fine-grained metapelite)	0.20	0.19	0.31	22	9	18	n.d.	n.d.	50	n.d.	1	n.d.
DM41Aqtz	Elongate-blocky quartz from open-fissure vein (FI assemblages F)												
DM41Bqtz	4 cm euhedral quartz crystal from open-fissure vein (FI assemblages F)												

Mineral abbreviations from Kretz (1983). The number in centimeter represents the distance of the rock sample form the open-fissure vein. The average data for KI and AI at Schiers was calculated from the samples in the table and 4 additional ones

qtz quartz sample

* crystallographic planes

Whole-rock geochemistry

Standard X-ray fluorescence (XRF) analysis was performed on fused glass beads prepared from rock powder mixed with lithium-tetraborate, using an X-ray fluorescence spectrometer (WD-XRF, Axios, PANalytical). The FeO content of the samples was determined at the University of Lausanne using wet chemistry and colorimetric methods (Johnson and Maxwell 1981; Wilson 1960). The carbon content in the samples was measured with a UIC Inc. CM 5012 CO_2 analyzer using coulometric titration. Total carbon is first combusted in a furnace (CM 5200 Autosampler) and subsequently introduced in the coulometer, whereas total inorganic carbon is determined by acid digestion (CM 5130). Total organic carbon is calculated as the difference between total carbon and inorganic carbon. Pressed powder pills from rock samples were prepared and analyzed with LA-ICPMS, to determine the concentrations of Li in both localities, and the major and trace-element composition for the samples from Schiers, which contain a high amount of carbonate. Concentrations were quantified based on the NIST 610 standard (5–7 measurements per sample).

Microthermometry

Fluid inclusion microthermometry was performed on quartz chips (500 and 1,000 μm thickness) using a Linkam THMSG-600 cooling-heating stage, attached to a Leitz optical microscope. For calibration, we used synthetic pure H_2O (final ice melting temperature: 0.0 °C, homogenization temperature: 374.1 °C) and CO_2 (final CO_2 ice melting temperature: −56.6 °C) fluid inclusions from SYNFLINC. Inclusions were cooled until −100 °C and then heated at a rate of 100 °C/min until −10 °C, 15 °C/min until −3, and 0.5 °C/min close to the final ice melting temperature. Total homogenization temperatures were measured by heating the fluid inclusions at a rate of 100 °C/min up to 115 °C, and then at 1 °C/min close to the homogenization temperature. The precision is about 0.1 °C for melting temperatures, and 0.5–1.0 °C for homogenization temperatures. Fluid inclusion densities and isochores were calculated with the FLUIDS software package (Bakker 2003), using the Zhang and Frantz (1987) equation of state for the H_2O–NaCl system.

LA-ICPMS microanalysis of fluid inclusions

Individual fluid inclusions were analyzed using a GeoLas laser ablation system (193 nm ArF excimer laser) connected to an ICP-quadrupole-MS (Perkin Elmer Elan 6100 DRC) (Günther et al. 1997; Heinrich et al. 2003). A small amount of H_2 (between 3 and 5 ml/min) was added to the Ar flow to increase the sensitivity for some elements without impairing others (Guillong and Heinrich 2007). For analyzing Ca, the ^{44}Ca isotope was used instead of ^{40}Ca, which has a very high background due to ^{40}Ar from the carrier gas. Although ^{44}Ca may be affected by interference from $^{28}Si^{16}O^+$ produced from ablation of quartz, the effect is small and can be adequately corrected by background subtraction. The uncertainty of this correction is counterbalanced by the improvement in counting statistics using the more abundant ^{44}Ca, compared with measuring the mass ^{42}Ca, which suffers from a higher background. For comparison, several fluid inclusion assemblages were also analyzed using a dynamic reaction cell (DRC), which allows the measurement of ^{40}Ca by suppression of the interfering ^{40}Ar. The concentration of Ca determined with the DRC was found to be identical within error, compared with measurements of Ca on mass ^{44}Ca without the DRC, but use of the DRC impairs the detection of some other elements. Element concentrations were quantified using the SILLS software package by deconvolution of host and inclusion signals (Guillong et al. 2008b). For most elements, NIST 610 was used as reference material. The concentrations of Br and Cl were quantified using the Sca-17 scapolite standard (Seo et al. 2011). The data obtained from each fluid inclusion were carefully screened, and only data with clearly visible peaks above $3\sigma_{\mathrm{background}}$ were considered for evaluation of concentrations. The limit of detection for the different elements varied as a function of the volume of the sampled inclusions, making it in some cases difficult to detect some elements that are present at low concentrations.

Phase equilibria computation

Pseudosections for bulk-rock compositions from Thusis were calculated in the system Na–K–Ca–Fe–Mg–Si–Al–O–H–C with the Perplex software (Connolly and Petrini 2002). The thermodynamic data came from the internally consistent thermodynamic database of Holland and Powell (Holland and Powell 1998, updated in version tc-ds55), and the fluid phase was modeled as H_2O–CO_2 mixture with the CORK equation of state (Holland and Powell 1991, 1998). The following activity-composition models were considered: OrFsp(C1), AbFsp(C1) (Holland and Powell 2003); Amph(DPW) (Dale et al. 2005); Anth, Bio(HP), Carp, Ctd(HP), hCrd, Cumm, Ep(HP), Gt(HP), O(HP), Opx(HP), St(HP), T, Do(HP), M(HP) (Holland and Powell 1998); Chl(HP) (Holland et al. 1998); and Mica(CHA) (Coggon and Holland 2002). Pressure–temperature pseudosections and mineral isopleth distributions were calculated using bulk compositions that were adjusted by subtracting TiO_2 (present below 1 %) and MnO. Mn was not considered in the calculations, because there is currently no activity-composition model to account for the presence of Mn in calcite- and dolomite-type carbonate solid solutions. The activity model for the fluid phase is restricted to molecular C–O–H mixtures and does not account for the small reduction in water activity due to the dissolved salts. Mineral abbreviations are after Kretz (1983).

Vein mineralogy and textures

Thusis

The foliation-parallel veins are filled with milky-white elongate-blocky quartz (definition of quartz microtextures after Bons and Jessell 1997) and coarse-grained calcite (later than quartz). The marginal zone of open-fissure veins is characterized by a 20–30-cm thick zone of elongate-blocky milky-white quartz that is intergrown with calcite (Fig. 4a). The elongate-blocky quartz contains wall-rock fragments which were partly transformed into chlorite (Fig. 4a, b). The vein center is partially filled with euhedral quartz crystals, which are overgrown by euhedral rhombohedral calcite crystals (Figs. 3, 4c, d). The euhedral quartz crystals have well-developed crystal faces and their sizes range from 1 to 20 cm. Most euhedral quartz crystals have prismatic morphology, but tabular and highly distorted crystals are common, which originated as fragments of fibrous or earlier blocky quartz that were later overgrown by euhedral quartz crystals (Fig. 4d). Fiber quartz has formed by a multitude of cracking and rehealing events (Ramsay 1980; Cox and Etheridge 1983; Fisher and Brantley 1992; Mullis 1996), and fluid inclusions trapped in fiber quartz closely represent the fluid from which the quartz crystallized (e.g., Mullis 1975, 1987; Mullis et al. 1994). Large euhedral crystals commonly show dark-gray 'phantom growth zones' in their interior, formed by microscopic fragments and mineral grains from the host metasediment deposited episodically onto upward-facing crystal faces during repeated deformation events affecting the fluid-filled cavity.

Chlorite is the main vein-forming sheet silicate mineral. Both the quartz close to the wall-rock contact and the euhedral crystals in the vein center enclose light-green patches of fine-grained vermicular chlorite, which form in various stages of progressive decomposition of wall-rock fragments. Identical chlorite is also found as thin layers on and between the euhedral quartz and calcite crystals. The presence of chlorite with comparable textures is widespread in Alpine fissure veins (Mullis 1996; Tarantola et al. 2007, 2009). Many euhedral quartz crystals show features of repeated fracturing and rehealing, and their upper surfaces are commonly covered with smaller quartz pieces, shale fragments, or fine-grained crystals of chlorite or cookeite.

Cookeite is the last mineral in the crystallization sequence and was identified by XRD and confirmed by semi-quantitative analysis of Li using LA-ICPMS. This trioctahedral lithium chlorite ($LiAl_4[AlSi_3O_{10}](OH)_8$) is locally present as a white layer of small platy crystals, and is always deposited on the surface of the quartz and calcite

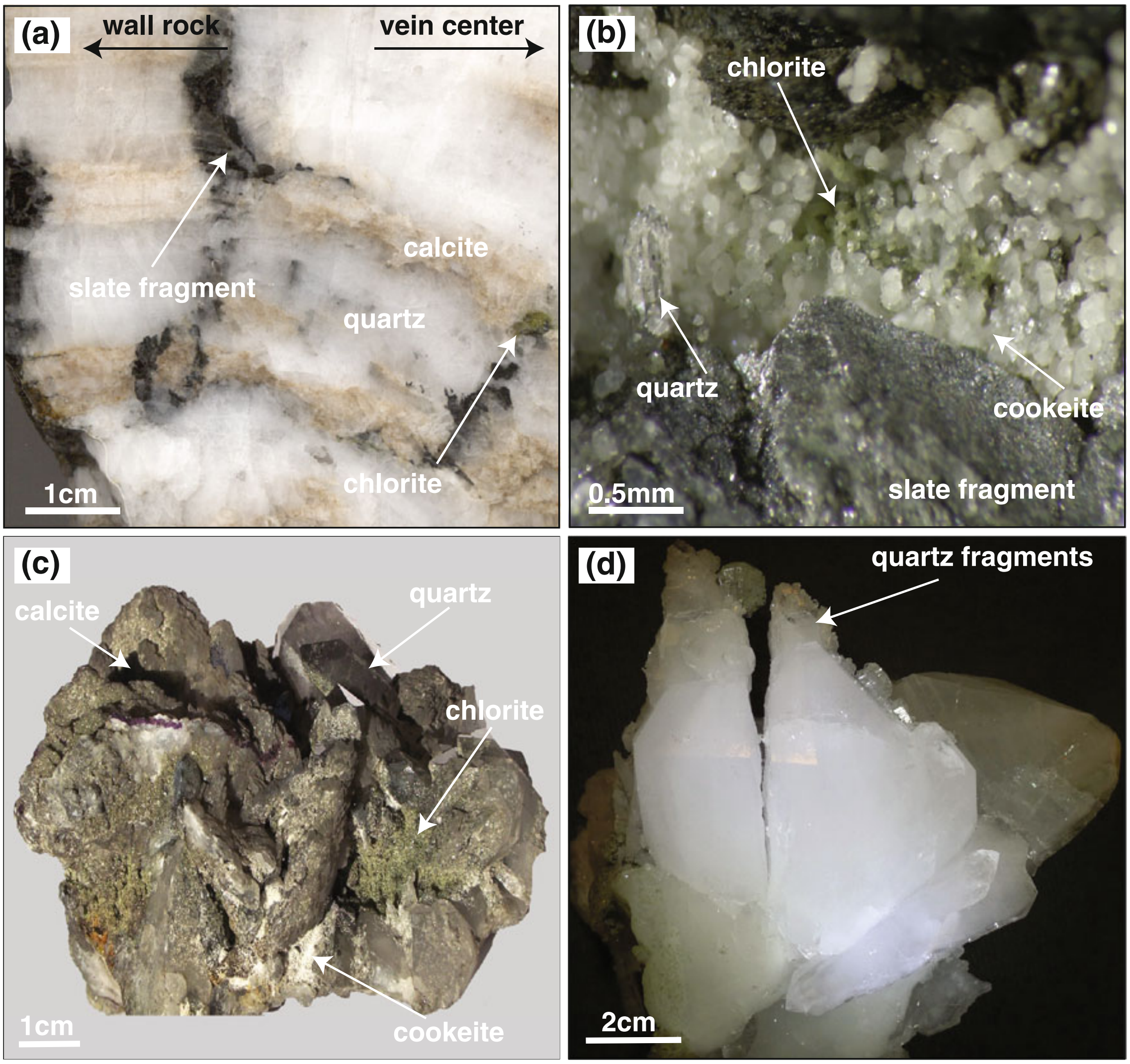

Fig. 4 Photographs illustrating the mineral assemblage, textural relationships, and paragenetic sequence of open-fissure veins at Thusis. **a** Slab of elongate-blocky quartz that has grown at the wall-rock contact. The quartz is intergrown with calcite and contains pockets of chlorite, as well as wall-rock fragments. **b** Detail of a layer of cookeite that has grown at the expense of chlorite. **c** Euhedral quartz crystals (from the central part of the vein), with coarse-grained calcite crystals on top. The euhedral quartz crystals are overgrown by a thin layer of chlorite followed by cookeite. **d** Euhedral quartz crystal which was fractured during the vein evolution and which has fragments of broken quartz crystals attached to sides, indicating multiple cracking and rehealing events

crystals or on rock fragments (Fig. 4b, c). The mineral appears as transparent crystals with pearly luster, up to 1 mm in size, which in some places seem to overgrow and replace chlorite (Fig. 4b). Cookeite is more commonly known as a hydrothermal alteration product of Li pegmatites, but was previously described from metapelites within the same mineral assemblage, although not in veins, of the Dauphinois zone in the Western Alps (Julien and Goffé 1993). The growth sequence in the open-fissure veins can be summarized as: early elongate-blocky quartz and coarse-grained calcite, followed by euhedral quartz with chlorite inclusions, rhombohedral calcite, then chlorite as thin layer covering the euhedral quartz crystals and finally cookeite.

Schiers

Both foliation-parallel and open-fissure veins are filled with quartz and coarse-grained calcite. Calcite makes up most of the vein filling in both vein types, followed by coarse-grained quartz. The open-fissure veins contain at least two generations of quartz and calcite. The first generation is present close to the wall-rock contact and is texturally coarse-grained and massive. The second generation of minerals crystallized in the center of the veins starting with quartz as prismatic euhedral crystals (1–5 cm in size), which is overgrown by rhombohedral calcite. No vein-forming sheet silicate minerals were observed at this locality.

Mineralogy and geochemistry of host rocks

The metasedimentary rocks that host quartz veins in the Thusis area show an intercalation of coarse and finer-grained layers (1–10 cm thick), reflecting variability in the proportions of the sand, silt, and clay components. Based on X-ray powder diffraction data, the most abundant mineral in the wall- and host-rock samples is quartz, followed by muscovite, chlorite, paragonite, and small amounts of clinozoisite, rutile, and carbonates (ankerite and calcite). The abundance of minerals from different samples determined by quantitative X-ray analysis is listed in Table 1. Bündnerschiefer samples from Schiers are more carbonate-rich and show pronounced bedding, defined by marly and sandy lithologies. The most abundant mineral is calcite, followed by quartz, muscovite, chlorite, and minor rutile.

Oriented samples were measured by XRD to determine the illite and chlorite crystallinity. Samples from Thusis have an average KI (from 22 measurements) of 0.239 ± 0.020 ($\Delta°2\theta$). The AI has an average value of 0.196 ± 0.012 ($\Delta°2\theta$) for plane (001) and of 0.186 ± 0.011 ($\Delta°2\theta$) for plane (002). Samples from Schiers have an average KI (from 6 measurements) of 0.293 ± 0.013 ($\Delta°2\theta$). The AI has an average value of 0.189 ± 0.010 ($\Delta°2\theta$) for plane (001) and of 0.192 ± 0.013 ($\Delta°2\theta$) for plane (002).

Carbonaceous material is present in both study areas. In the Thusis samples, CM could be observed as a residue after dissolving the samples in hydrofluoric acid. CM is present as lath-shaped grains up to 1 mm in length, intergrown with muscovite and chlorite. Average values for the parameter R2 and R1 were 0.68 ± 0.04 and 2.79 ± 0.33, respectively. In the Schiers samples, disordered CM (Lahfid et al. 2010) is present as irregular grains up to 1 mm in length, in the interstices between calcite, quartz, and muscovite grains. Raman spectra of disordered CM from Schiers show considerably wider bands around 1,100–1,400 cm^{-1} and around 1,500–1,600 cm^{-1}.

The major and trace-element composition of wall- and host-rock samples is summarized in Table 2. Samples from Thusis show variable SiO_2 concentrations, in the range of 43–67 wt%, reflecting different proportions of sand, silt and clay components. Aluminum is essentially correlated with the Si concentration. The total iron content ranges between 5.7 and 10.4 wt%, and the $FeO/(FeO + Fe_2O_3)$ ratios are between 0.39 and 0.66. Inorganic carbon concentrations are between 0 and 1.59 wt%, and those of organic carbon are between 0.4 and 0.96 wt%. There is no correlation between the CM (organic carbon) and the FeO content, but there is a clear correlation between the Ca content and inorganic carbon, indicating that most of the Ca is bound to carbonate minerals (mainly calcite). The Li concentrations are in the range of 135–208 ppm. Samples from Schiers show an average SiO_2 content from 43 to 47 wt% and an average Al content from 7.1 to 8.4 wt%. CaO varies between 36 and 41 wt%, reflecting the presence of large modal amounts of carbonates. The total iron content ranges between 2.7 and 3.4 wt%, and the $FeO/(FeO + Fe_2O_3)$ ratios are between 0.46 and 0.50. Inorganic carbon concentrations are around 6 wt% and those of organic carbon are between 0.13 and 0.28 %. The Li concentrations are lower than in the samples from Thusis, in the range of 57–88 ppm.

Fluid inclusion results

Inclusion petrography

Thusis

Fluid inclusion assemblages were studied from both vein generations. Inclusions have sizes of 20–300 μm (Fig. 5), which make it possible to analyze both major and trace

Table 2 Whole-rock geochemical data for wall- and host-rock samples from Thusis and Schiers

Sample Locality	DM3	DM13	DM14	DM15	DM16 Thusis	DM18	DM17	DM19	DM24	DM30* Schiers	DM38*
wt%											
SiO_2	55.0	54.3	45.7	62.5	49.0	52.2	66.8	46.1	43.6	43.67	47.04
TiO_2	0.79	0.79	0.95	0.69	0.75	0.88	0.55	1.16	1.24	0.38	0.44
Al_2O_3	22.4	21.3	24.0	17.5	19.4	23.3	15.1	28.9	32.1	7.15	8.45
Fe_2O_3	4.16	5.13	4.60	2.31	4.47	3.30	3.07	4.33	3.48	1.34	1.60
FeO	3.14	5.29	5.56	4.51	4.27	3.96	2.63	4.52	2.23	1.34	1.95
MnO	0.24	0.41	0.71	0.40	1.12	0.41	0.31	0.29	0.01	0.11	0.10
MgO	2.57	3.31	3.66	2.20	3.52	2.68	2.03	2.88	2.77	1.42	1.75
CaO	1.35	0.60	2.20	1.08	4.03	1.52	1.50	0.29	0.33	41.71	36.12
Na_2O	1.12	0.66	0.92	0.56	0.73	1.36	0.67	1.49	2.86	0.40	0.61
K_2O	3.39	2.74	3.50	2.79	2.98	3.51	2.27	4.20	4.55	1.78	1.89
P_2O_5	0.10	0.14	0.15	0.10	0.11	0.10	0.08	0.11	0.19	0.69	0.06
LOI	5.8	5.33	8.03	5.20	9.77	6.94	4.99	5.92	6.57		
C_{inorg}	0.30	0.14	0.78	0.35	1.59	0.50	0.41	0.02	0	6.20	5.60
C_{org}	0.52	0.44	0.55	0.51	0.40	0.91	0.59	0.70	0.96	0.28	0.13
Total	100.1	100.0	100.0	99.9	100.2	100.1	100.0	100.2	99.9	100.0	100.0
Ppm											
Rb	181	147	193	152	168	188	123	220	222	111	131
Ba	440	366	498	359	430	467	280	559	796	281	303
Sr	273	159	224	142	218	301	178	310	286	1,496	1,065
Nb	17	15	18	14	16	18	14	25	27	9	10
Zr	129	148	181	129	142	166	98	193	204	30	39
Hf	5.5	4.8	6.3	4.1	5.4	5.4	4.0	6.3	7.0	0.9	1.0
Y	14	31	39	23	28	47	20	18	11	21	15
Ga	37	38	42	31	37	38	27	46	49	13	15
Zn	150	185	182	120	156	144	114	172	140	67	67
Cu	97	88	139	131	93	103	76	113	109	18	19
Ni	128	154	164	102	124	121	81	165	106	35	38
Co	33	32	32	51	37	41	30	32	13	7	11
Cr	115	132	157	107	139	132	82	162	220	63	80
V	145	159	185	132	160	158	102	205	243	85	126
Sc	22	21	24	17	19	19	12	26	23	9	11
La	41	32	29	22	28	41	24	35	51	22	15
Ce	76	60	75	51	62	78	38	99	60	58	34
Nd	32	27	31	24	28	32	20	39	26	35	15
Pb	77	46	48	49	45	55	46	47	45	12	17
Th	15	14	18	14	14	19	11	21	26	14	5
U	0.8	1.8	1.7	1.0	2.7	0.9	2.2	3.3	2.3	1.2	1.1
Li	164	182	209	135		209	155			57	88
Be	4.0	3.1	3.5	3.1		5.5	4.0			1.9	1.9
Ge	3.0	5.1	4.6	5.6		3.2	2.9			2.7	0.7
As	17	5	18	9		10	22			4	5
Mo	0.3	0.3	0.6	0.8		0.6	0.5			0.4	0.2
Sn	5.1	6.5	6.9	5.7		7.7	5.3			2.5	2.7
Sb	1.5	1.1	2.1	0.9		1.5	1.7			<0.4	0.7
Cs	13	13	18	15		23	12			8	10

* Samples analyzed only by LA-ICPMS on pressed powder pills

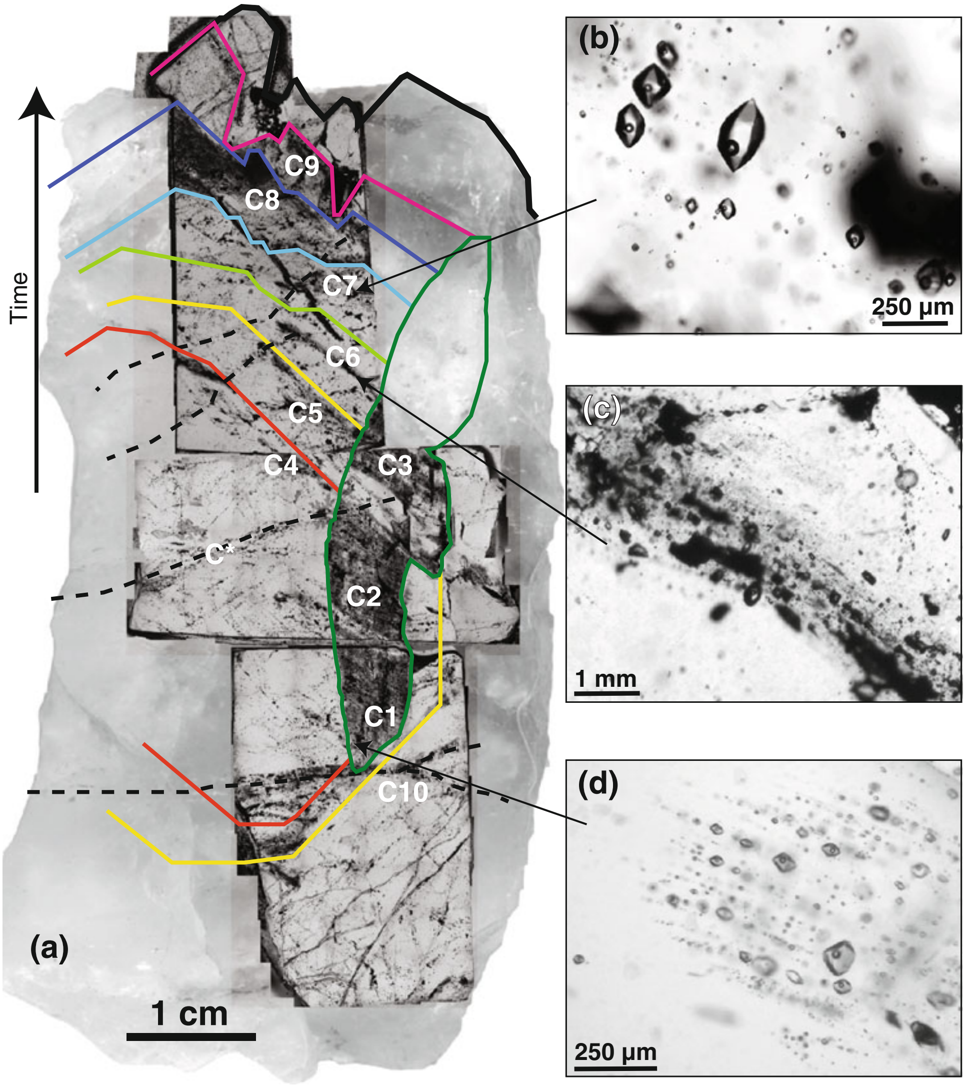

Fig. 5 **a** Fluid inclusion map of a large euhedral quartz crystal (background) that formed in the center of the open-fissure vein at Thusis, depicting different quartz generations (*solid lines*) and some secondary FI trails (*dotted black lines*). The *solid lines* represent quartz growth zones (*C4–C9*) delineated by solid inclusions of chlorite and carbonaceous matter on the quartz growth surfaces. Growth zones show a symmetric growth toward both sides of the crystal. The central part of the crystal (area with green boundaries) is composed of early fiber quartz that was overgrown by the euhedral quartz. In each quartz growth zone, several FIA were analyzed. Fluid inclusion assemblages *C1–C9* are related to different sequential growth zones, whereas assemblages *C10* and *C** represent late secondary FI trails that crosscut the quartz crystal. **b** Example of two-phase aqueous fluid inclusions in one of the outer growth zones. **c** Trail of fluid inclusions associated with solid inclusions of chlorite and carbonaceous matter. **d** Several subparallel fluid inclusion trails in the fiber quartz (*C1–C3*)

elements with LA-ICPMS, at a sensitivity and precision that are better than in all earlier studies of low-salinity fluids. Fluid inclusions from foliation-parallel veins have sizes from 20 to 60 μm and no clear relative time sequence could be established for the analyzed assemblages, as all inclusions are of identical petrographic appearance in multiple cross-cutting trails (assemblages A1–A5; Fig. 6). The inclusions are aqueous two-phase (liquid–vapor), with a calculated density of 0.95–0.97 g/cm^3. Fluid inclusions from open-fissure veins were measured from early elongate-blocky quartz close to the wall rock, and from euhedral quartz crystals close to the vein center, which enclosed and overgrew broken fragments of quartz generations with intermediate position in the growth history of the vein (Fig. 4d). In the elongate-blocky quartz, the fluid inclusions are aligned on several subparallel trails, which have the same orientation as the foliation of the wall rock (assemblages B; Fig. 6). The studied euhedral quartz crystals (e.g., Fig. 5) commonly enclose fragments of earlier quartz and show later zones containing abundant solid inclusions of chlorite and carbonaceous matter, which trace the consecutive growth zones of the quartz crystals.

Fig. 6 Summary of the average composition of fluid inclusion assemblages determined by LA-ICPMS (data from Thusis and Schiers) with error bars representing the standard deviation of each FIA. Data reported include the average element concentrations (ppm), the Cl/Br molar ratio, and average estimated trapping temperatures using the Na–Mg and Li–Mg solute geothermometers (Giggenbach 1988; Kharaka and Mariner 1989). Assemblages *A* are from the foliation-parallel quartz veins (Thusis), *B–E* are assemblages from the open-fissure veins (Thusis) and *F* are assemblages from open-fissure veins (Schiers). Data from the open-fissure veins (Thusis area) are further subdivided based on textural relationships. *B* are assemblages from elongate-blocky quartz close to the wall-rock contact, and *C1–C10* are assemblages from different quartz generations and growth zones of a single large euhedral quartz crystal. Assemblages *C1* and *C3* are hosted by fiber quartz, *C4–C9* are hosted by different growth zones of euhedral quartz overgrowing the fiber quartz, and *C10* and *C** represent late secondary FI trails that crosscut the quartz crystal. Assemblages *D* and *E* are from two other euhedral quartz crystals from the same vein

▶

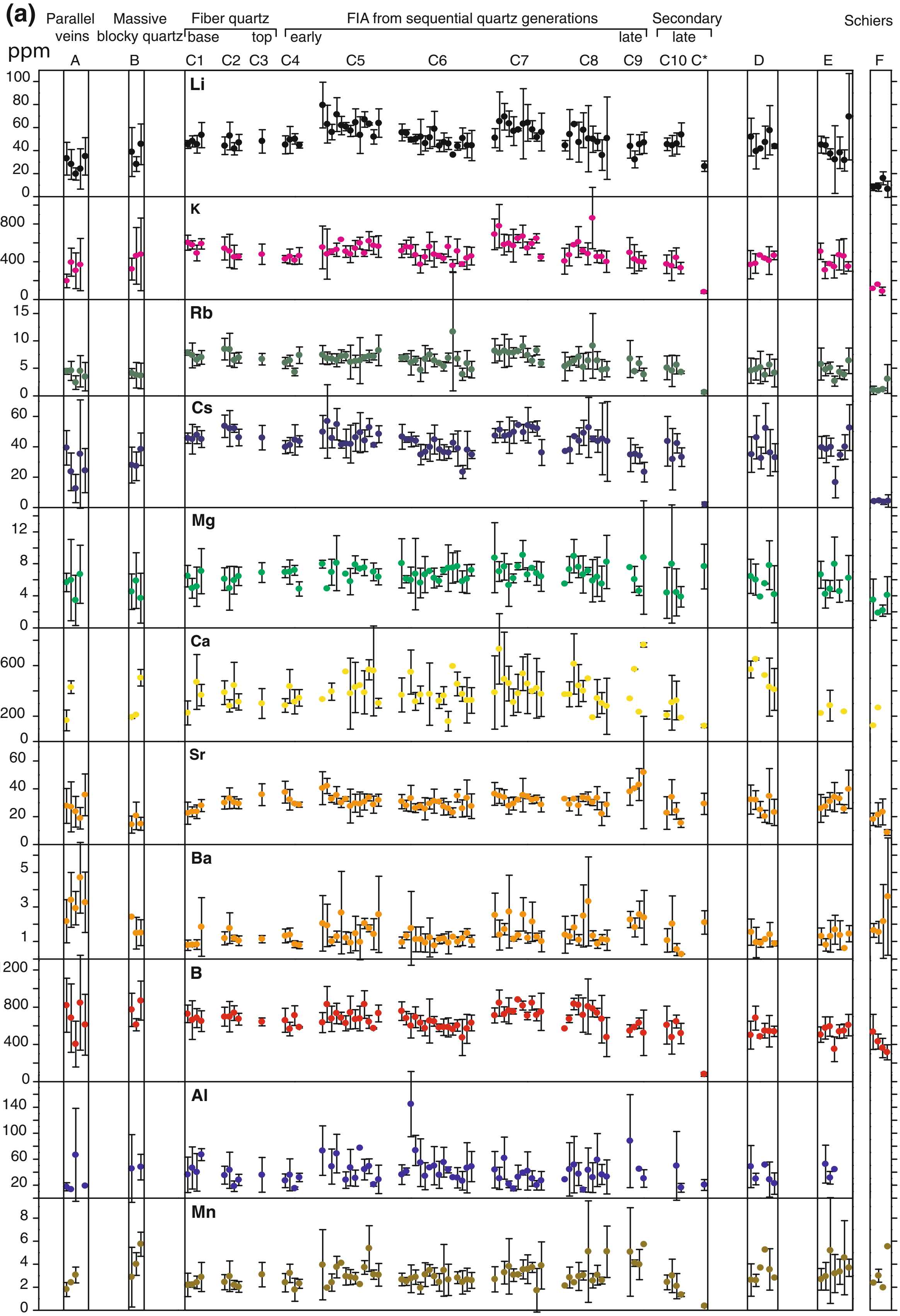
(a)
ppm
Parallel veins
Massive blocky quartz
Fiber quartz
base
top
FIA from sequential quartz generations
early
late
Secondary
late
Schiers
A
B
C1
C2
C3
C4
C5
C6
C7
C8
C9
C10
C*
D
E
F
Li
K
Rb
Cs
Mg
Ca
Sr
Ba
B
Al
Mn
100
80
60
40
20
0
800
400
0
15
10
5
0
60
40
20
0
12
8
4
0
600
200
0
60
40
20
0
5
3
1
1200
800
400
0
140
100
60
20
8
6
4
2
0

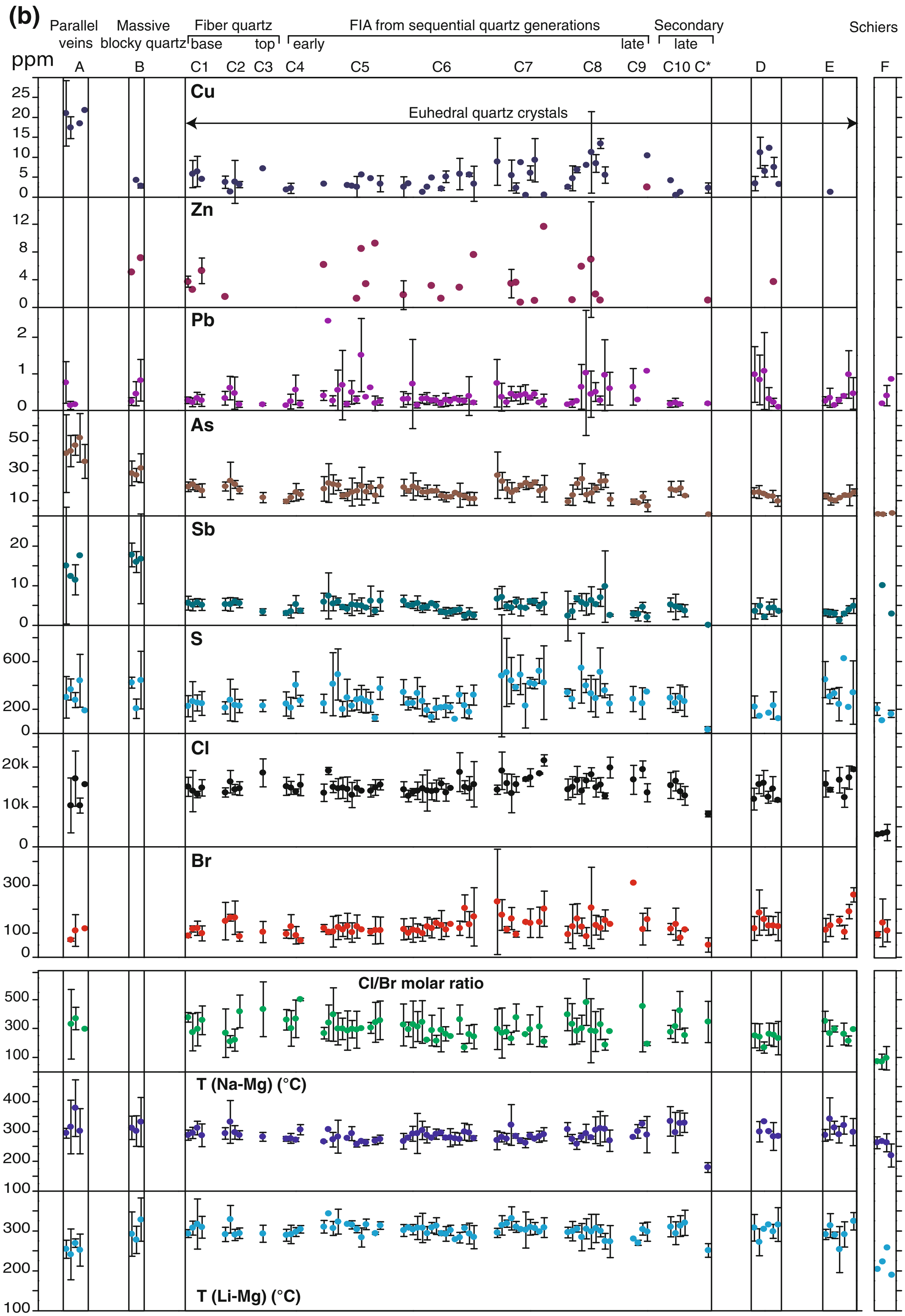

Fig. 6 continued

Numerous fluid inclusions are aligned with the solid inclusions and are interpreted as primary FIAs, but most FIAs are (pseudo-)secondary trails along healed fractures. These relations allow a partial deduction of the relative sequence of fluid entrapment, as exemplified in Fig. 5. The naming convention of the fluid inclusion assemblages in Table 3 conforms to the numbering of the quartz growth zones and inclusion generations in relative chronological order (e.g., FIA C4–C9; Fig. 5). In addition to numerous FIA from one large euhedral quartz crystal, FIA from two other crystals were analyzed for comparison (D and E). Results showed that all fluid inclusions in the open-fissure veins are aqueous two-phase (liquid–vapor) inclusions of indistinguishable composition and density. In approximately 30 % of the inclusions, black and sometimes semi-transparent solid inclusions (platy crystals) could be observed as accidentally entrapped phases.

Microthermometry and Raman results

Fluid inclusions from the foliation-parallel veins had temperatures of final ice melting of −2.3 ± 0.1 °C. Their initial ice melting temperature could not be determined. Fluid inclusions from the open-fissure veins had temperatures of final ice melting between −2.5 ± 0.1 and −2.2 ± 0.1 °C (for all FIA, independent of inclusion size, including assemblages from the elongate-blocky quartz and the euhedral crystals). The maximum variation of ±0.1° in any single assemblage is within the reading precision of the cooling-heating stage. Because of the partly large inclusion sizes, initial ice melting temperatures could be measured and they were close to −23 °C, indicating the presence of fluids in the NaCl–H_2O system (Goldstein and Reynolds 1994).

The salinity was calculated from the final ice melting temperature, and ranges between 3.7 and 4.0 wt% equivalent NaCl (Bodnar 1993). The total homogenization temperatures were in the range of 136–140 °C for foliation-parallel veins. For the open-fissure veins, the homogenization temperatures have an average of 138 °C for fluid inclusions in the elongate-blocky quartz and of 130 °C for the inclusions in the euhedral quartz crystals. The standard deviation in a given assemblage was less than ±5 °C, which is only slightly higher than the precision of the instrumental calibration. A single fluid inclusion assemblage (C*) that was present on a late-stage secondary trail was found to have a final ice melting temperature of −1.0 °C, but its homogenization temperature was still consistently around 134 °C.

Clathrate was identified in very large inclusions as a transparent phase of low refractive index. The amount of clathrate present in the inclusions was estimated using several cooling-heating cycles (for inclusions with sizes larger than 50 μm) and was found to be less than 0.1 vol %. The presence of clathrate in such low amounts results in an estimate for the volume fraction of CO_2 of less than 0.03 vol%, which should not detectably affect the melting temperature of ice or the determination of the trapping temperature (Goldstein and Reynolds 1994). The final clathrate melting temperatures ranged from −0.6 to −0.2 °C (10 inclusions of different assemblages).

The presence of trace amounts of CO_2 in fluid inclusions from the euhedral crystals was confirmed by Raman spectroscopy. The vapor bubble and the aqueous phase were analyzed separately in 10 large inclusions. Raman bands for gaseous CO_2 were visible at 1,283.1 and 1,385.8 cm^{-1} in the vapor bubble, and at 1,273.8 and 1,380.8 cm^{-1} in the liquid phase. The density of CO_2 in the bubble could be calculated using the difference between the positions of the two Fermi diad bands from the equation of Fall et al. (2011), yielding an average value of 0.019 g/cm^3. Minor amounts of CH_4 and N_2 were also detected in the vapor phase, based on sharp bands at 2,916 and 2,327.3 cm^{-1}, respectively. Mole fractions for the gases present in the vapor bubble were calculated from the relative areas of the corresponding molecule peaks in the Raman spectra (Burke 2001). The average values are 0.920 ± 0.006 for CO_2, 0.071 ± 0.002 for N_2, and 0.009 ± 0.007 for CH_4. No CH_4 or N_2 bands could be observed in the Raman spectra of the liquid phase, and no solid phases could be detected in the fluid inclusions. These observations confirm that gas species are present in very low amounts and do not have any significant impact on the calculation of salinity and density (Goldstein and Reynolds 1994).

Schiers

Fluid inclusions assemblages were studied from the open-fissure veins in the massive quartz (first generation) and the euhedral quartz crystals (second generation). Their size is around 10–30 μm and different assemblages do not show clear time relationships. The inclusions are two-phase (liquid–vapor) aqueous inclusions, with an average density around 0.98 g/cm^3. The final melting temperature of ice was in the range of −1.0 to −0.9 °C, with very consistent values for a given FIA. Salinities were calculated as 1.6–1.7 wt% eqv. NaCl (Bodnar 1993). The homogenization temperature ranged between 82 and 87 °C, with very consistent values within one FIA and also between different assemblages. No clathrate melting could be observed, and no volatile species were detected by Raman spectroscopy.

Elemental composition of fluid inclusions

A total number of 526 individual fluid inclusions were analyzed by LA-ICPMS, belonging to 97 FIA with 2–16 inclusions per assemblage. The results are illustrated in Fig. 6 and representative values for each quartz generation are summarized in Table 3. The complete dataset with the results for all individual inclusions is available as supplementary electronic material. The analyzed elements (Li, Na, K, Rb, Cs, Mg, Ca, Sr, Ba, B, Al, Mn, Cu, Zn, Pb, As, Sb, Cl, Br, and S) have very consistent concentrations within a given assemblage, with relative differences being typically on the order of 20–40 %.

FIA from Thusis have very similar element abundances for the successive vein types, as well as for different quartz crystals, growth zones, and fluid inclusion generations in the open-fissure vein. All fluid inclusion compositions are clearly dominated by NaCl, with K and Ca being present in minor concentrations of 310–860 and 160–760 ppm. The concentrations of the other alkali (Li, Rb, Cs) and earth alkaline (Mg, Sr, Ba) elements are typically one to two orders of magnitude lower than K and Ca. The fluid inclusions contain considerable amounts of B (350–880 ppm) and S (120–630 ppm), whereas the concentrations of base metals (Cu, Zn, Pb) are rather low (less than 10 ppm for the open-fissure vein). The overall variability is somewhat greater for the ore metals Cu, Zn, and Pb. The elements Cu, As, Sb, and Ba show distinct differences between vein types and quartz generations. Their concentrations are typically higher in the FIA from the foliation-parallel veins and from the elongate-blocky quartz in the open-fissure veins. The concentrations of Cu are 20 ± 2 ppm in FIA from the foliation-parallel veins, compared with 5 ± 3 ppm in FIA from the open-fissure veins. Li shows the opposite trend, with concentrations being higher in the assemblages from the late euhedral quartz crystals. The Al concentration varies between 13 and 88 ppm among assemblages (ignoring one outlying value), and the average value is 41 ± 19 ppm for all FIA.

FIA from Schiers show substantially lower concentrations of most elements compared with Thusis, being correlated with the lower salinity. The only exceptions are Mn, Sb, Ba, Pb, and Br, which have average concentrations that are similar to the FIA from Thusis. Because of the considerably smaller FI size, Al could not be analyzed in samples from Schiers, being below the 10-ppm average limit of detection. The Fe concentration was always below the limit of detection, estimated to be less than 7–20 ppm for FIA from euhedral quartz crystals from Thusis and less than 35 ppm for the quartz vein samples from Schiers. The Cl/Br ratios could be measured with rather good precision (30 %). The Cl/Br molar ratios are distinctly different between samples from Thusis and Schiers, with average values of 280 ± 70 for all measured FIA from Thusis and 70 ± 20 for the FIA from Schiers.

Temperatures calculated with the empirical Na–Mg solute geothermometer (Giggenbach 1988) are 291 ± 25 °C for the samples from Thusis, distinctly higher than the temperature of 252 ± 22 °C obtained for the samples from Schiers. The Li–Mg solute thermometer (Kharaka and Mariner 1989) gave temperatures of 298 ± 19 °C for Thusis and 219 ± 30 °C for Schiers.

In few individual FI, the LA-ICPMS measurements yielded concentrations for some elements that were much higher than the assemblage average and their time-resolved signal did not follow the Na signal. This was a clear indication that a solid phase has been accidentally trapped in the fluid inclusions. Based on the suite of elements that had increased concentrations in a single FI, muscovite, chlorite, and iron sulfide solid inclusions appear to be the most likely candidates. Muscovite inclusions resulted in an increase in Al and K to more than 100 times of the assemblage average, whereas chlorite inclusions caused a simultaneous increase in Al, Mg, and Fe. All elements determined in the fluid inclusions were continuously monitored in the quartz matrix hosting the FI during ablation. Most elements were found to be below the detection limit, but quartz contained an Al concentration of 6 ± 2 ppm and a Li concentration of 0.3 ± 0.1 ppm. Only the quartz matrix hosting few FIA in the latest growth zones of euhedral quartz crystals had somewhat higher Al concentrations up to 24 ppm. This was accounted for with the matrix correction procedure (Guillong et al. 2008a, b).

Discussion

Significance of fluid compositions

The analyzed element concentrations are clearly representing the elements present in the fluid inclusions, as demonstrated by the excellent consistency within individual FIA. Due to the relatively large size of the analyzed inclusions (mostly larger than 50 µm), the detection limits were typically at least one order of magnitude lower than the measured element concentration. The presence of accidentally trapped phases in few fluid inclusions was always detected in the time-resolved ICMPS signals, typically associated with a large simultaneous increase in a group of elements compared with the assemblage average (typically by half to one order of magnitude). The elements that were truly present in solution clearly followed the Na signal in the time-resolved ICPMS signals. When accidentally trapped solid inclusions were detected, the resulting data were excluded from further consideration.

The amount of Al analyzed in individual inclusions is close to the assemblage average for most FIA, and the time-resolved Al signal closely follows the signals of other elements present in solution (including the large Na peak). When the Al peak in the time-resolved signal was

Table 3 Average elemental composition, Cl/Br ratios, final ice melting temperature, temperature of total homogenization, and Na–Mg and Li–Mg solute geothermometer temperatures of representative fluid inclusion assemblages (FIA)

FIA	Nr.FI	Li (ppm)	Na (ppm)	K (ppm)	Rb (ppm)	Cs (ppm)	Mg (ppm)	Ca (ppm)	Sr (ppm)	Ba (ppm)	B (ppm)	Al (ppm)	Mn (ppm)
Thusis: foliation-parallel veins													
A2	4	28	15,300	390	4.5	24	6	430	27	3.4	680	13	2.4
SD		13		150	1.7	12	5.1	50	18	1.6	370		
Thusis: extension veins cross-cutting the foliation (elongate-blocky quartz)													
B3	9	45	14,600	480	3.6	38	3.7	500	15	1.5	870	48	5.7
SD		6		300	2.3	9	3.5		10	0.9	70		1.0
Thusis: extension veins cross-cutting the foliation (euhedral quartz crystals)													
C1–4	7	53	15,700	590	7	45	7.1	370	28	1.8	650	67	2.9
SD		11		50	1.2	6	2.8	90	4	1.7	110	9	1.3
C2–1	10	44	15,700	540	8.5	54	6.1	390	30	1.2	700	35	2.4
SD		8		120	2.0	7	1.4	90	5	0.4	100	14	0.7
C3	5	48	15,700	480	6.7	46	6.9	300	36	1.1	640	36	3.1
SD		10		110	1.1	8	1.2	120	8	0.2	40	27	1.1
C4–2	16	49	15,200	460	6.4	41	7	430	32	1.4	560	36	3.2
SD		12		80	1.0	5	1.5	130	7	0.4	70	25	0.8
C5–8	13	64	14,300	540	6.3	46	7.9	430	30	1.5	670	31	2.8
SD		12	500	80	1.1	9	1.1	200	6	1.0	100	12	0.5
C6–7	6	51	15,700	560	7.5	40	7.1	370	29	1.2	650	47	3.5
SD		9		150	1.1	9	0.1	250	4	1.1	240		0.5
C7–4	7	63	15,800	590	7.8	48	5.3	460	28	2.7	760	21	3.8
SD		11	200	90	2.5	12	2.7	140	6	2.1	140	5	2.4
C8–8	7	47	16,400	450	6.4	44	6.4	340	33	0.9	740	59	3
SD		7		60	1.6	7	2.5	150	8	0.3	50	41	0.8
C9–4	4	47	16,400	400	3.8	23	8.8	760	52	2.4	520	30	5.7
SD		9	200	70	1.1	7	7.1	20	40	1.6	240	14	
C10–3	8	46	15,200	440	5.6	42	4.4	320	24	0.5	640	50	2.1
SD		9		110	1.7	6	2.9	150	6	0.3	70	53	1.1
C*	6	26	7,500	80	0.6	2	7.7	120	29	2.1	80	20	0.4
SD		5		10	0.3	1.6	2.8	10	8	0.7	20	8	0.1
D2	7	39	15,900	380	4.8	46	6	650	32	0.9	680	29	2.6
SD		15		100	1.9	14	1.9	10	7	0.9	130	9	0.5
E2	9	44	15,800	310	4.8	38	4.2		27	0.8	580	52	2.9
SD		7	200	90	1.1	9	1.8	50	7	0.4	120	29	1.2
Schiers: open-fissure veins													
F2	7	8	7,500	160	0.9	4.6	1.9	260	21	1.5	430		3
SD	4				0.8			9	0.6	80		0.6	

FIA	Nr.FI	Cu (ppm)	Zn (ppm)	Pb (ppm)	As (ppm)	Sb (ppm)	S (ppm)	Cl (ppm)	Br (ppm)	Cl/Br (molar)	$\mathrm{Tm}_{\mathrm{ice}}$ (°C)	$\mathrm{Th}_{\mathrm{total}}$ (°C)	$T_{\mathrm{Na-Mg}}$ (°C)	$T_{\mathrm{Li-Mg}}$ (°C)
Thusis: foliation-parallel veins														
A2	4	17		0.1	43	12	370	10,300	70	330	−2.3	138	315	241
SD		3		0.1	10		90	6,900	10	106		3	90	63
Thusis: extension veins cross-cutting the foliation (elongate-blocky quartz)														
B3	9	2.8	7.1	0.8	32	17	440				−2.2	138	331	328
SD				0.3	4	3	80				0.1	1	51	34
Thusis: extension veins cross-cutting the foliation (euhedral quartz crystals)														
C1–4	7	4.5	5.3	0.3	17	5.1	250	14,700	100	330	−2.4		286	309

Table 3 continued

FIA	Nr.FI	Cu (ppm)	Zn (ppm)	Pb (ppm)	As (ppm)	Sb (ppm)	S (ppm)	Cl (ppm)	Br (ppm)	Cl/Br (molar)	Tm_{ice} (°C)	Th_{total} (°C)	$T_{Na–Mg}$ (°C)	$T_{Li–Mg}$ (°C)
SD			1.9	0.2	4	1.4	100	2,000	30	44	0.1		38	27
C2–1	10	3.7	1.5	0.3	19	5.3	210	13,600	150	200	−2.4	133	293	291
SD		1.5		0.2	3	1.6	50	1,100	80	74	0.1		19	18
C3	5	7.2		0.2	12	3.4	230	18,500	100	420	−2.4	130	282	293
SD				0.0	3	0.8	50	3,500	50	84	0.1	1	15	21
C4–2	16	2.2		0.2	12	3.5	210	14,800	130	260	−2.3	135	276	291
SD		1.3		0.2	3	1.6	90	1,600	50	55	0.1		16	23
C5–8	13	2.6	1.3	0.3	16	5	280	14,700	130	250	−2.2	130	257	304
SD		2.6		0.1	5	1.4	90	2,000	50	56	0.1		9	9
C6–7	6	4.8	3.1	0.3	16	5.5	140	13,900	120	260	−2.3	131	278	308
SD				0.1	1	0.4	40			47			1	13
C7–4	7	5.4	3.4	0.5	15	4.4	440	13,300	160	190	−2.4	125	322	331
SD		3.8	2.1	0.2	7	1.7	190	4,800	50	19		2	68	29
C8–8	7	13	1	0.3	23	7	510	15,500	120	290	−2.5	134	310	300
SD		1.2		0.1	5	2.2	200	1,700	40	47		4	58	15
C9–4	4	10	17	1.1	7	2	340	13,500	160	190	−2.5	136	289	298
SD					3.9	1.1		2,300	50	6	0.1	1	61	24
C10–3	8	1.2		0.2	18	4.4	300	13,800	80	390	−2.4		328	312
SD				0.0	5	0.9	100	2,000	30	58	0.1		42	26
C*	6	2.2	1	0.2	0.9	0.3	30	8,200	50	390	−1.1	134	179	251
SD		1.3		0.0	0.6	0.01	20	700	30	63		1	17	17
D2	7	11		0.8	16	4.9	140	15,600	180	200	−2.4	136	299	272
SD		3.9		0.7	4	2.0		2,300	90	41		1	34	34
E2	9	1.2		0.3	11	3	310	14,300	130	250	−2.4	130	342	313
SD				0.3	4	1.0	60	600	50	40		1	71	30
Schiers: open-fissure veins														
F2	7			0.2	0.9	10	110	3,300	140	70	−1	87	267	223
SD	4			0.6			300	100	24	50	0.1	4		

Assemblage from foliation-parallel veins (A2), foliation cross-cutting open-fissure veins with elongate-blocky quartz (B3), and euhedral quartz (groups C, D, E), and from Schiers (group F2)

Nr.FI Number of fluid inclusions per assemblage, *SD* standard deviation

displaced compared with other elements (like Na, Li, B, Cs) or unusually high, Al values were associated with an increase in other elements (K, Fe, Mg), this indicated the presence of accidentally entrapped solids and the Al data were not used. The observation that the amount of Al is very constant within any measured FIA supports the conclusion that the Al is indeed present in solution. The Al concentration in the quartz matrix ranges from 0.2 to 10 ppm, which is substantially lower than in the fluid inclusions. Because the Al concentration is continuously monitored during ablation of the host quartz prior to breaching the fluid inclusion, Al contributed from the host quartz is subtracted by the background correction procedure. Post-entrapment modification of the Al concentrations due to diffusion from the surrounding quartz would appear possible, but is highly unlikely when temperature-dependent diffusion rates are considered. The diffusion coefficient for Al in quartz is around 1.9 μm^2 per 10^6 years at 400 °C, decreases strongly with temperature, and is substantially lower if Li is present in the quartz lattice (Cherniak 2010). Therefore, considering that the host quartz contains Li and that formation temperatures were well below 400 °C, we do not expect that the Al concentration was modified after entrapment of the FI.

Wall-rock alteration

The variations in the host-rock composition largely reflect the original abundance of sand, silt, and clay components related to more coarse- and fine-grained layers (Potter et al. 1963; Bhatia and Crook 1986; Wagner and Jochum 2002). There was no visible wall-rock alteration surrounding the studied quartz veins and immediate wall rocks have essentially the same mineralogy and whole-rock composition as the host metapelites, according to XRD and bulk-rock analytical data. Wedge diagrams (Ague 2011) can be used to test for possible chemical alteration effects in the wall rocks surrounding the larger open-fissure vein (Fig. 7). The compositional variability observed in these diagrams appears to be mainly caused by the original chemical heterogeneities in the host rocks, that is, major and trace-element variations that are correlated with the SiO_2 and Al_2O_3 concentrations. This does not exclude the possibility of a weak alteration (in particular, mobilization of silica from the wall rocks surrounding the veins), masked by the chemical variability of the host-rock precursor. All observations (no visible halo, no chemical leaching, or enrichment) suggest that the degree of alteration was comparatively low and that the fluid that infiltrated the vein-wall-rock system was close to equilibrium with the metasedimentary wall rocks. Alternatively, the absence of pronounced alteration features could reflect that the fluid flow was not highly focused and weak alteration affected a larger volume of rock. The foliation-parallel veins are widespread in the metasedimentary rocks, suggesting a larger scale of fluid migration. This interpretation would be in agreement with recent analysis of a large body of whole-rock compositional data from the Bündnerschiefer, where large-scale depletions during progressive metamorphism were only detected for a few elements, notably B, Li, and possibly Si (Garofalo 2011).

Composition and source of fluids

The chemical composition of the fluid inclusions is exceptionally homogenous despite the textural complexity of quartz precipitation during continued small-scale deformation. This indicates that the concentrations of most

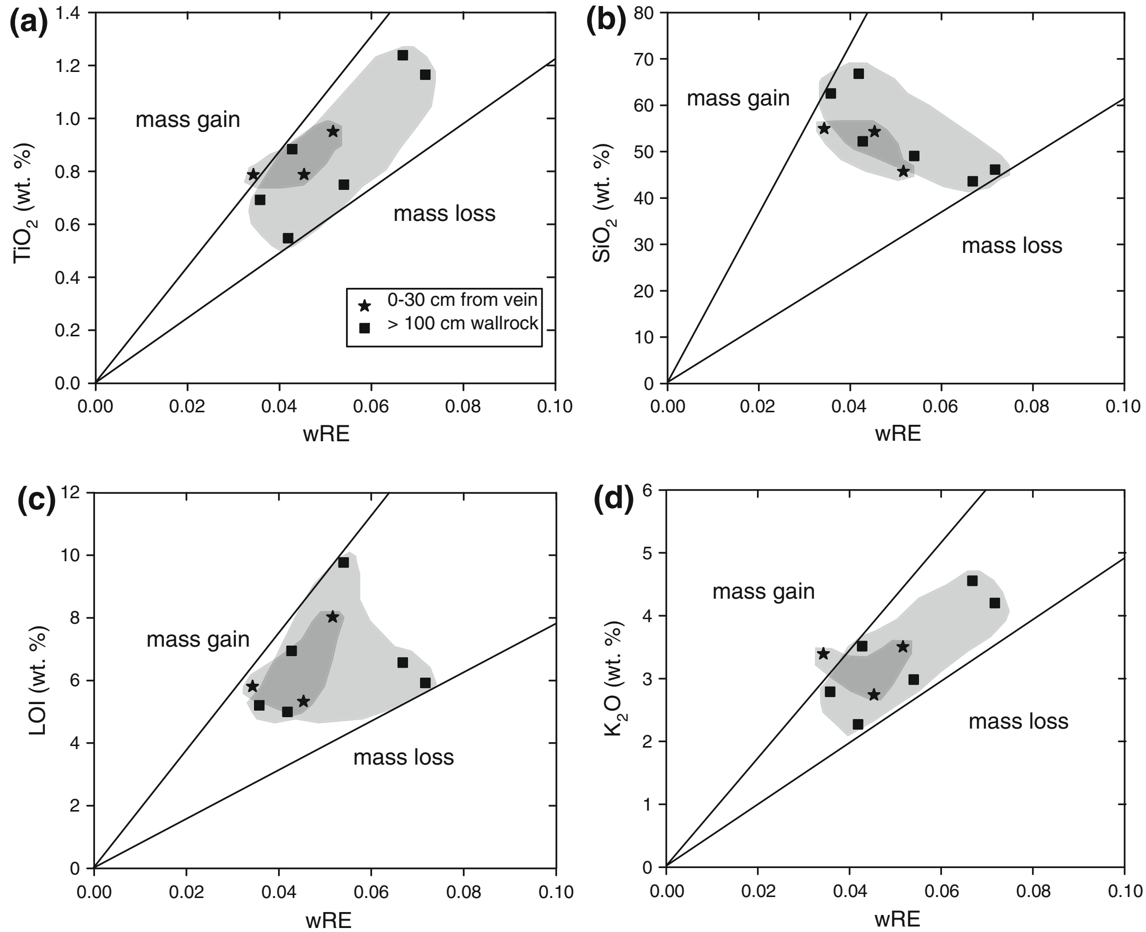

Fig. 7 Wedge diagrams (Ague 2011) plotting **a** TiO_2, **b** SiO_2, **c** loss on ignition (LOI), and **d** K_2O against weighted residual elements (wRE). The weighted residual elements represent an immobile element reference frame that is used to determine the changes in concentrations of mobile elements. The wRE was calculated from concentrations of Zr, Th, and U. The two lines define the primary compositional variability of the host-rock and the compositional reference frame for relative mass changes during fluid-rock interaction. Wall-rock samples enriched in mobile elements should plot above the upper line of the wedge, and samples depleted in that element below the lower line

elements are controlled by fluid-rock equilibrium, with trapping temperature (obtained from solute geothermometry), fluid bulk salinity, and the wall-rock composition being the dominant factors. When comparing fluid compositions from Thusis with those from Schiers, some elements such as Mn, Pb, Ba, and Br are present in similar concentrations, whereas many elements (Li, K, Rb, Cs, Mg, Sr, and As) have clearly lower concentrations in the fluids from Schiers. The bulk salinity of the FI in the veins from Schiers is approximately half of those in the veins from Thusis, resulting in lower concentrations of elements that are dominantly complexed by chloride (Wood and Samson 1998; Yardley 2005). In addition, the trapping temperatures of the FI in Schiers were at least 50 °C lower, resulting in lower solubility of most rock-forming elements. Ca does not show lower concentrations in the FI from Schiers, reflecting that fluid-rock exchange reactions involving quartzo-feldspathic rocks produce fluid compositions that are increasingly more calcic with decreasing temperature (Dolejs and Wagner 2008).

The presence of N_2 in percentage amount was reported by Andersen et al. (1993) from fluids contained in high-pressure rocks. In the majority of their analyzed inclusions, the N_2 had Raman bands at 2,327.7 cm^{-1} similar to the results of this study where the N_2 band was observed at 2,327.3 cm^{-1}. The presence of N_2 although in small concentrations could point to partial derivation of the vein-forming fluids from a high-pressure fluid.

The average molar Cl/Br ratio in the fluids from Thusis (280) is about half of the seawater value of 640 (McCaffrey et al. 1987) (Fig. 8), and the molar Cl/Br values from Schiers are even lower (70). The Cl/Br ratios could be explained by an origin of fluid salinity from brines that were produced by strong seawater evaporation (Fig. 8), which was then diluted by water released by metamorphic dehydration reactions. Seawater that was first evaporated to a 20-fold salinity (McCaffrey et al. 1987) and then diluted about 10 times would have 1.2 wt% Na, 2.1 wt% Cl, 135 ppm Br, and a molar Cl/Br ratio of 350, approximating the analyzed fluid composition of the Thusis inclusions. An alternative possibility to explain the high relative Br values (and Cl/Br values below seawater) would be a Br contribution liberated from the organic matter (Kendrick et al. 2011) during dehydration of the Bündnerschiefer metasediments.

The observation that the samples plot below the 1:1 line in the Na/Br vs. Cl/Br diagram (Fig. 8a) indicates that they have an Na excess compared with (Cl + Br) of approximately 10 % on a molar scale. This can be explained by the presence of other ligands in the fluid inclusions that would balance the cation charge, most likely a combination of bicarbonate, sulfate, bisulfide, and borate. The B concentrations in FIA from the quartz veins are around 60 times higher compared with a fluid derived from evaporated seawater. The most likely source for the additional B would be fluid-rock interaction with the metasediments of

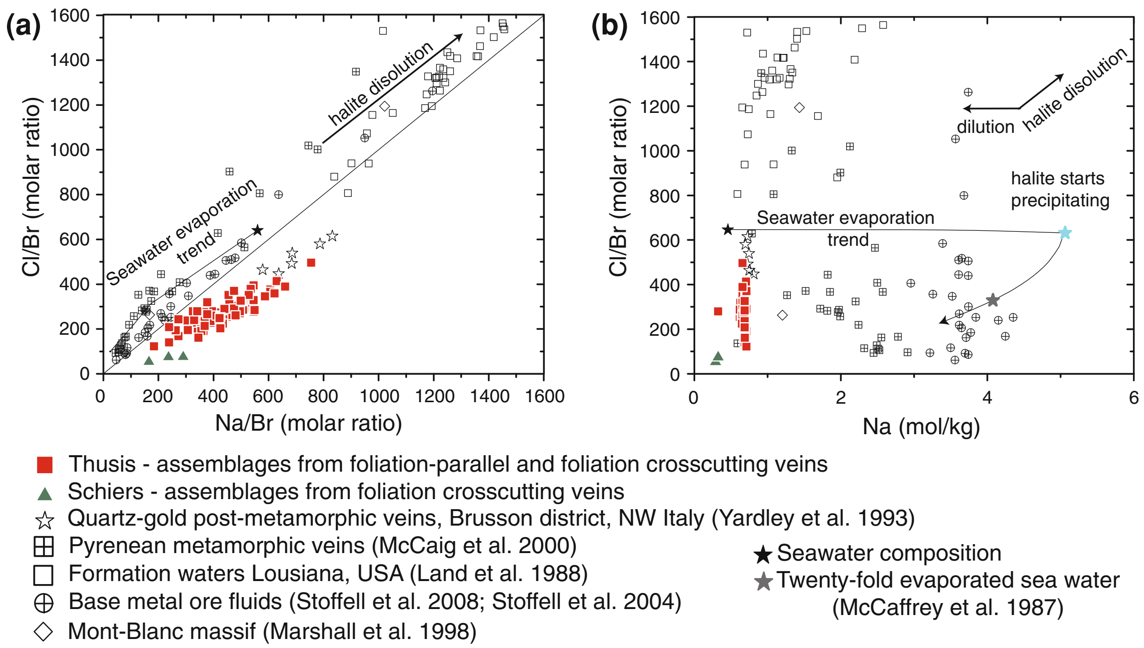

Fig. 8 **a** Fluid compositions from metamorphic veins from Thusis and Schiers, plotted onto an Cl/Br vs. Na/Br diagram. The samples are located below the 1:1 Cl:Na ratio, indicating the presence of additional anions such as bicarbonate. **b** Fluid compositions plotted in Cl/Br vs. Na space. For comparison, the composition of seawater, the seawater evaporation trend, and data for metamorphic fluids, formation waters and ore fluids are plotted as well

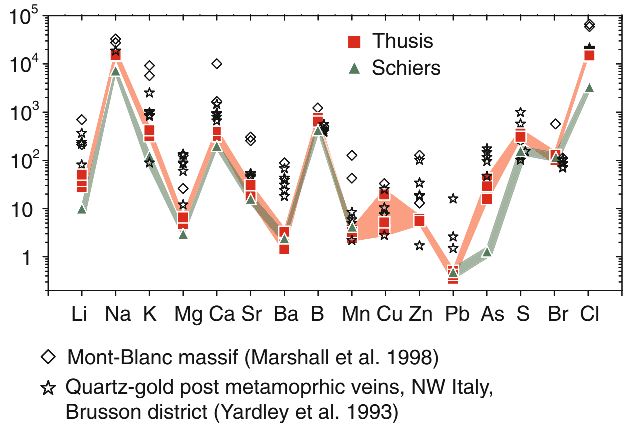

Fig. 9 Spider diagram comparing the element concentration data of fluid inclusions from the present study (average compositions from Thusis and Schiers) with data from other metamorphic settings. Fluid inclusions from the Mont-Blanc massif have a salinity of 5–12 wt% and trapping temperatures of 260–370 °C (Marshall et al. 1998). Fluid inclusions from the quartz-gold veins in the Brusson (Monte Rosa) district have a salinity of 4.5–5 wt% and trapping temperatures of 230–300 °C (Yardley et al. 1993)

the Bündnerschiefer. The average B concentration in the metapelites is around 100 ppm (Spivack et al. 1987). Boron is mostly hosted by illite (substituting for K) and is released during the destruction of the illite structure up to greenschist facies conditions (Reynolds 1965; Wunder et al. 2005), becoming available to metamorphic fluids expelled by the metasediments. B together with Li and SiO_2 were identified as chemical components that are substantially mobilized during prograde regional metamorphism of the Bündnerschiefer (Garofalo 2011). The rather high concentrations of B in the analyzed fluids would suggest that this element was largely removed from the host rocks.

The fluid data of this study (Fig. 9) show close similarity to the composition of ore fluids from the post-metamorphic lode-type gold-quartz veins in the Brusson (Monte Rosa) district, NW Italy (Yardley et al. 1993; crush-leach method) and similar Cl/Br ratios indicate a comparable fluid source. It has been proposed that metamorphic devolatilization of Bündnerschiefer sediments has generated the ore fluids that were responsible for the formation of the Brusson gold district (Pettke et al. 2000). Compositional data from other metamorphic fluids (Fig. 9) show larger variations in element abundance, total salinity, and proportions of CO_2 reflecting host-rock heterogeneity, different temperature–pressure conditions of fluid-rock reaction, and volumetrically different contributions of externally derived fluids (McCaig et al. 2000).

Metamorphic pressure–temperature conditions

The pressure–temperature conditions are constrained from several independent metamorphic indicators, using a multi-method approach (e.g., Lanari et al. 2012). Based on the Kübler Index, the boundary between the anchizone (subgreenschist facies) and epizone (greenschist facies) is defined at a value of 0.25 (Kübler and Jaboyedoff 2000). The boundary for the Árkai Index is at 0.26 and 0.24 for the (001) and (002) basal reflections of chlorite (Árkai et al. 1996). Samples from Thusis are therefore located at the boundary between the anchizone-epizone and the lower epizone (lower greenschist facies). Paragonite was observed in the samples and can result in higher uncertainty in determining the KI (Doublier 2010), but paragonite present in subordinate amounts compared with illite/muscovite should not have an important effect on the (001) basal reflections (Árkai et al. 2003). For chlorite, the values from Thusis are lower than the boundary of anchizone-epizone and indicate clearly epizone conditions. Most studies placed the anchizone-epizone boundary between 270 and 350 °C (Árkai et al. 2000, 2003; Frey 1987b; Merriman and Frey 1999; Wang et al. 1996). The KI results from Schiers (0.29) point to a lower grade compared with Thusis and are characteristic for high anchizone conditions (subgreenschist facies, 250–280 °C; Mullis et al. 2002).

The carbonaceous material Raman spectra of host-rock samples from Thusis show a low D2 band intensity (resulting in an asymmetric G band) and a slight shift of the band to higher wavelengths, characteristic for temperatures above 300 °C (Aoya et al. 2010). The D bands (1,100 and 1,800 cm^{-1}) grow in intensity relative to the G band with increasing degree of disorder in the graphitic structure (Sadezky et al. 2005). Raman spectra from Thusis are similar to the spectra of CM that has been metamorphosed at temperatures around 330–340 °C (Beyssac et al. 2002, 2003; Aoya et al. 2010). Using the two well-calibrated CM geothermometers, the resulting temperatures for the Thusis host- and wall-rock samples are 328 ± 18 °C (Beyssac et al. 2003) and 338 ± 18 °C (Aoya et al. 2010). These temperature estimates are in good agreement with the illite crystallinity data (270–350 °C). The CM Raman spectra of the host-rock samples from Schiers have D and G bands of similar intensities and a symmetric G band, pointing to distinctly lower metamorphic conditions compared with the Thusis area. The samples from Schiers have CM Raman spectra that are similar to the ones described for the temperature range 250–300 °C (Lahfid et al. 2010). The 250–300 °C temperature interval is in good agreement with the illite crystallinity data (250–280 °C).

Comparing the mineral assemblages observed in wall-rock samples from Thusis with pseudosection calculations results in temperature–pressure estimates of 290–350 °C and 2.8–3.8 kbar (Fig. 10). Clinozoisite and the absence of wairakite constrain pressures at values higher than 2.5 kbar (around 300 °C; Fig. 10a). To better constrain the pressure and temperature conditions in the rocks, the mineral modes

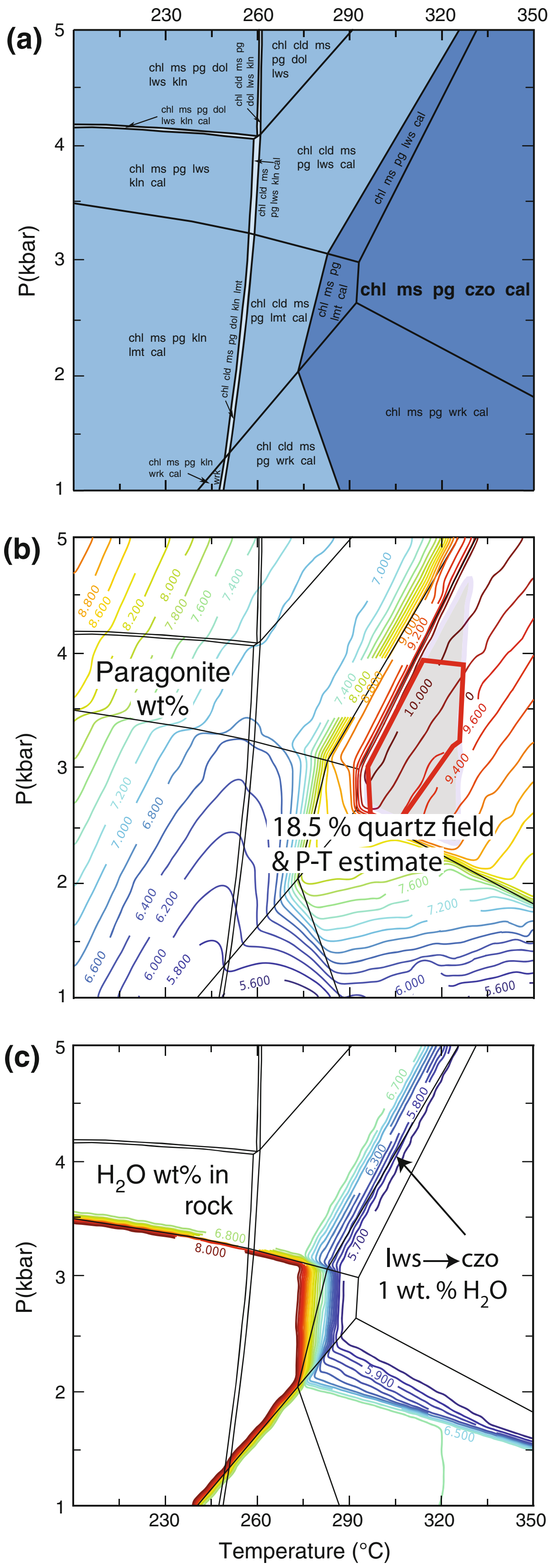

◀**Fig. 10** **a** Example of pressure–temperature pseudosection (sample DM14). **b** Mineral mode distribution diagrams for paragonite (wt%) with the 18.5 wt% quartz field (*gray*) and P–T estimate (*red*). **c** Calculated H_2O amount present in the rock as function of pressure and temperature. The lawsonite (to clinozoisite) breakdown reaction results in a decrease in the H_2O concentration from 6.7 to 5.7 wt%, corresponding to fluid production of about 1 wt%

predicted from Perplex calculations (e.g., Fig. 10b) were compared with the quantitative XRD data for each sample. For temperatures and pressures of 290–350 °C and 2.8–3.8 kbar, the mineral assemblage and modes predicted for different samples match those of the XRD data. Plotting the amount of H_2O contained in minerals in P–T space (Fig. 10c) shows that the stability field of the mineral assemblage chl + ms + pg + czo + cal + qz is bounded by dehydration/hydration reactions. This suggests that along the prograde part of the P–T path substantial amounts of fluid will be released, which would result in increase in fluid pressure and formation of mineral veins.

Several samples of chlorite, which was observed to crystallize as one of the late minerals in the open-fissure veins from Thusis, were analyzed using LA-ICPMS (data provided as supplementary electronic material). The chemical composition is quite constant with less than 2 wt% variation in SiO_2. Although the empirical chlorite geothermometers (Cathelineau 1988) have been controversially discussed (de Caritat et al. 1993; Essene and Peacor 1995), the calculated average temperature (6 analyses) of 301 ± 17 °C is in good agreement with the other temperature indicators discussed above. Chlorite with vermicular texture was often found present on trails along with fluid inclusions, making it possible to link them directly with the analyzed fluids. Cookeite, the mineral which crystallized last in the open-fissure veins at Thusis, can be utilized as an indicator of minimum formation temperature. Based on phase equilibria experiments, the stability field of the cookeite + quartz assemblage is limited to 280–450 °C, at pressures of 1–14 kbar (Vidal and Goffé 1991).

Temperatures determined using the Na–Mg and Li–Mg solute geothermometers for the FIA from Thusis are close to the wall-rock metamorphic indicators. The Na–Mg thermometer gives slightly lower temperatures for FIA in the elongate-blocky quartz and the euhedral quartz crystals from the later generation of open-fissure veins, compared with the maximum temperature conditions estimated for the wall rock. This suggests that the veins probably formed closely after the peak of the greenschist metamorphism. The Na–K geothermometer (Giggenbach 1988) gave unreasonably low temperatures, consistent with the absence of feldspars in the buffering assemblage of the wall rocks. Conversely, the wall-rock mineral assemblage composed of chlorite, paragonite, and cookeite forms a

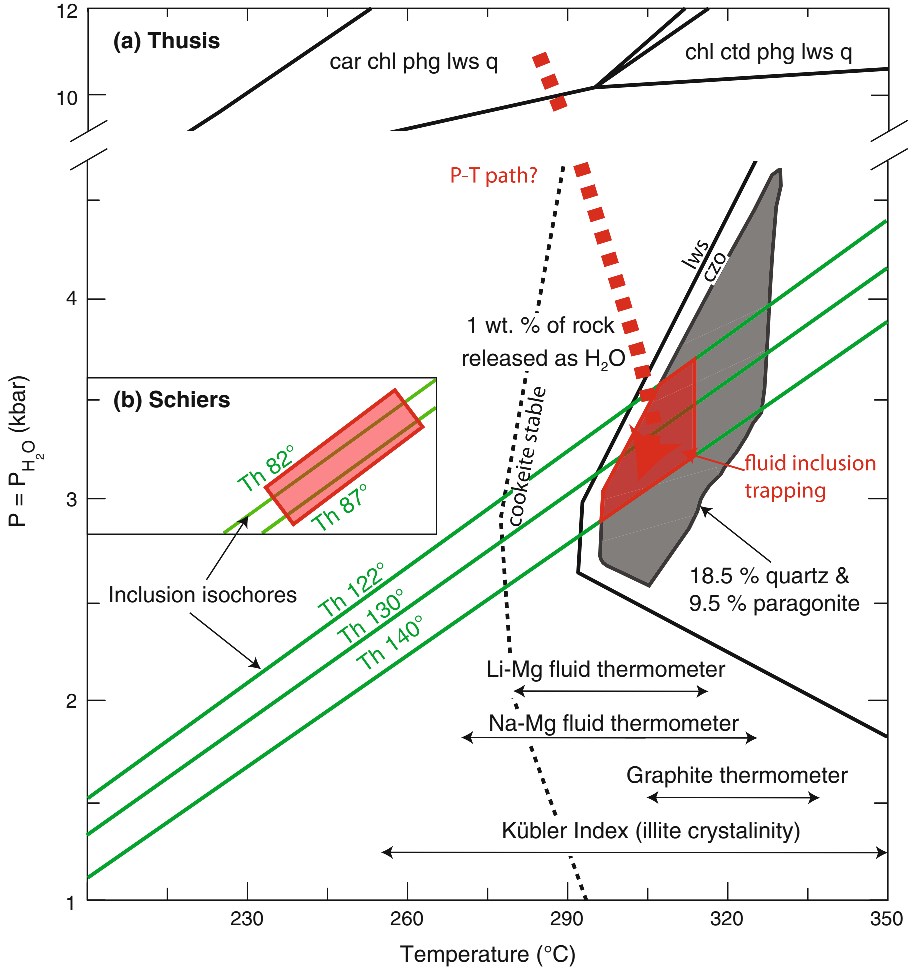

Fig. 11 **a** Pressure–temperature diagram illustrating the P–T ranges estimated for the Barrovian metamorphism of the wall rocks and of the vein formation events for Thusis. The diagram is based on summary of different P–T indicators, including illite crystallinity, graphite thermometry, cookeite stability (Vidal and Goffé 1991), mineral stability fields and mineral mode distributions from pseudosection modeling, Na–Mg and Li–Mg fluid geothermometry, and fluid inclusion isochores. The area where all metamorphic indicators for the wall-rock samples overlap represents the best estimate for the metamorphic conditions. The *dashed red line* shows the inferred P–T path. **b** Inferred formation conditions of the open-fissure veins at Schiers, based on intersection of FI isochores with trapping temperature estimated form the solute geothermometry

buffering assemblage for Na–Mg and Li–Mg exchange, and resulted in consistent temperatures for both solute thermometers. Compared with the Thusis data, solute geothermometry gave approximately 50–70 °C lower temperatures for FIA from quartz veins in Schiers. Average temperatures are 252 ± 14 and 219 ± 30 °C for the Na–Mg and Li–Mg thermometer, respectively. These are in good agreement with the temperature estimates from the illite crystallinity data and the Raman spectra of CM. Temperatures determined for the open-fissure veins in the Schiers area are thus at the lower end of the pressure–temperature conditions estimated for the host rocks.

Finally, FI isochores were calculated and combined with the independent geothermometers to constrain the pressures of fluid inclusion entrapment (Fig. 11). The concentrations of dissolved Ca and K relative to Na are small, and volatile gas species such as CO_2, N_2, and CH_4 are only present in minor amounts. Therefore, these additional components should not have a detectable effect on the density and isochore calculation (Goldstein and Reynolds 1994). Taking into account the complete range in measured homogenization temperatures (Th: 122–140 °C), the resulting P–T conditions for quartz veins from Thusis are in the range of 290–320 °C and 2.8–3.8 kbar (Fig. 11a). For FIA hosted in quartz veins from Schiers (Fig. 11b), the corresponding trapping temperature and pressure would be 252 ± 14 °C and 3.3–3.4 kbar. Assuming the fluid pressure as essentially lithostatic (and taking the average rock density as 2.7 g/cm^3), the inferred pressures at the time of vein formation correspond to 10.6–14.3 km depth for Thusis and around 13 km for Schiers. From the calculated depth and the P–T conditions, the geothermal gradients are obtained as 22–27 and 19–20 °C/km for the Thusis and Schiers area, respectively. The P–T conditions derived in this study are in good agreement with data from low-grade metamorphic rocks in the Falkins nappe (around 20 km NW of Schiers). From combination of illite crystallinity, coal rank, and fluid inclusion data, P–T conditions of 226–249 °C and 2.3–4.2 kbar were obtained (Frey et al. 1980). Agard et al. (2000) conducted a study on fluid inclusions in syn-metamorphic vein segregations from the Schistes Lustrés. They analyzed FI belonging to the HP-LT metamorphic stage with salinities from 0 to 15 wt% eq. NaCl, and FI belonging to the subsequent greenschist facies (from chlorite bearing veins) had uniform salinities around 3.7 wt% eqv. NaCl.

The consistency of host-rock thermometry and fluid inclusion solute geothermometers and isochores indicates that the vein fluid composition was controlled by rock-dominated chemical equilibria in all respects with the possible exception of the external origin of fluid salinity. This is clear evidence for the attainment of fluid-rock equilibrium at conditions close to the greenschist metamorphic peak. The open-fissure was also physically in hydrological equilibrium with the rock. It was kept open by lithostatic fluid pressure through parts of the dehydration and deformation history of the mechanically rather incompetent host rocks, while quartz crystals in the interior of the fissure were broken and recrystallized in open space to form multiple generations of overgrowing crystals surrounded at all sides by crystal facets. The fissure was an almost closed fluid pocket in the sense that flow through the open cavity must have been slow enough that even clay-sized particles liberated by wall-rock deformation settled exclusively on upward-facing crystal surfaces. These well-equilibrated fluids were well preserved because the Bündnerschiefer rocks have a rather low permeability, and progressive deformation has continuously destroyed any permeability of the host rocks that was created due to volume loss by devolatilization. Therefore, the fluids were preserved during the retrograde exhumation path.

Geodynamic implications

The rocks of the Bündnerschiefer represent marine sediments which were subducted at high pressures, followed by continental collision and nappe stacking. The accretion wedge experienced first a high-pressure low-temperature (blueschist facies) metamorphism at conditions of a low geothermal gradient characteristic for subduction zones (Baldwin et al. 2004) indicated by the presence of carpholite assemblages in the same rock unit close to Thusis (Bousquet et al. 1998; Engi 2011; Wiederkehr et al. 2011). During decompression to greenschist facies conditions (36–29 Ma), some areas experienced an increase in geothermal gradient, resulting in an increase in temperature and a pervasive overprint of the high-pressure assemblages by greenschist facies metamorphism (Wiederkehr et al. 2009). In the Thusis area, the paleogeothermal gradient increased from lower values (5–10 °C/km) during the post-high-pressure decompression stage to values of 22–27 °C/km, as determined from isochores of the fluid inclusions analyzed in this study (associated with greenschist facies metamorphism). We interpret that the resulting pressure–temperature path advanced from the carpholite field (Fig. 11a), and then crossed the lawsonite-clinozoisite dehydration reaction during decompression, resulting in substantial fluid production that gave rise to formation of metamorphic quartz veins.

Following decompression due to collision and nappe stacking, the rocks were affected by a Barrovian metamorphic overprint, from greenschist to amphibolite metamorphic grade (Frey and Ferreiro Mählmann 1999; Ferreiro Mählmann et al. 2002; Wiederkehr et al. 2009, 2011; Berger et al. 2011; Engi 2011). The observation that the fluids record P–T conditions close to peak metamorphism (greenschist overprint) to slightly retrograde indicates that the final exhumation must have been very fast or that decompression occurred essentially along the FI isochores. Otherwise the fluid inclusions should have experienced density re-equilibration during the retrograde path and one should observe abundant secondary FI assemblages that would record late retrograde conditions.

Conclusions

1. Accretionary-wedge metasediments of the Bündnerschiefer experienced metamorphic dehydration and the formation of Alpine fissure veins at 320 ± 20 °C and 2.8–3.8 kbar (Thusis), and 250 ± 20 °C and 3.4 ± 0.5 kbar (Schiers area). The apparent geothermal gradient (T/P) is higher in Thusis compared with Schiers, which is in accordance with their relative position in the wedge. Thusis is located closer to the thermal dome in the Lepontine area (Frey and Ferreiro Mählmann 1999), whereas Schiers is further away from this thermal anomaly and immediately underlies the cold overriding Adriatic plate (Austro-Alpine nappe).
2. Petrological pressure–temperature estimates from the host rocks are in excellent agreement with solute geothermometry based on analyzed FI compositions, indicating that the open-fissure veins formed during decompression close to peak metamorphic temperatures. This situation is different compared with areas closer to the Lepontine dome (Central Switzerland) where the fissure veins are retrograde compared with peak amphibolite-facies metamorphism (Mullis et al. 1994), and record several late-stage fluid flow events.
3. The solute composition of the FI reflects fluid-rock interaction with the surrounding host rocks, and element concentrations are mainly controlled by salinity as well as trapping temperature and pressure. The fluid originated from dehydration reactions caused by the breakdown of lawsonite. Measured concentrations of most elements in the studied FI assemblages are at the lower end of typical concentration ranges, when compared with other metamorphic and crustal fluids. Variations of element concentrations in these metamorphic fluids are rather small, and the fluid

composition does not show the large variability of typical magmatic and ore deposit-related fluids.

4. Consistency between pseudosection modeling and mineral assemblages and modes, in conjunction with the observation that all metamorphic indicators predict the same P–T conditions, demonstrates that the metamorphic fluid has approached chemical equilibrium with the surrounding wall rocks.

Acknowledgments Thierry Adatte and Hans-Rudolf Pfeifer are thanked for assistance with standardization of illite crystallinity measurements and giving us access to ferric/ferrous iron analysis at the Centre d'Analyse Minérale at the University of Lausanne. Lydia Zehnder (ETH Zurich) has helped with the XRD and XRF measurements and Thomas Good is thanked for making the fluid inclusion sections. Thanks are due to Michael Plötze for helping with the quantitative determination of the minerals by XRD, and to Mark Caddick for the introduction to Perplex. We thank Wilfried Winkler for insightful discussions about the regional geology of the study area and for helping with sample preparation for the illite crystallinity study. The fissure vein at Thusis was discovered by Michael Heinrich along with Phoebe Härtner and Dimitri Meier, who all contributed with observations about the three-dimensional geometry of the mineral occurrence. We also thank Jakob Schumacher and the Council of the village of Tschappina for logistical support with our field work. Constructive comments by Josef Mullis, Jaques Touret, and three anonymous reviewers are gratefully acknowledged.

References

Agard P, Goffé B, Touret JLR, Vidal O (2000) Retrograde mineral and fluid evolution in high-pressure metapelites (Schistes lustrés unit, Western Alps). Contrib Mineral Petrol 140:296–315

Ague JJ (1994) Mass transfer during Barrovian metamorphism of pelite, south-central Connecticut. I. Evidence for changes in composition and volume. Am J Sci 294:989–1057

Ague JJ (2003) Fluid flow in the deep crust. In: Heinrich DH, Karl KT (eds) Treatise on geochemistry. Pergamon, Oxford, pp 195–228

Ague JJ (2011) Extreme channelization of fluid and the problem of element mobility during Barrovian metamorphism. Am Mineral 96:333–352

Andersen T, Austrheim H, Burke EAJ, Elvevold S (1993) N_2 and CO_2 in deep crustal fluids: evidence from the Caledonides of Norway. Chem Geol 108:113–132. doi:10.1016/0009-2541(93)90320-I

Aoya M, Kouketsu Y, Endo S, Shimizu H, Mizukami T, Nakamura D, Wallis S (2010) Extending the applicability of the Raman carbonaceous-material geothermometer using data from contact metamorphic rocks. J Metam Geol 28:895–914

Árkai P, Merriman RJ, Roberts B, Peacor DR, Toth M (1996) Crystallinity, crystallite size and lattice strain of illite-muscovite and chlorite; comparison of XRD and TEM data for diagenetic to epizonal pelites. Eur J Mineral 8:1119–1137

Árkai P, Mata MP, Giorgetti G, Peacor DR, Toth M (2000) Comparison of diagenetic and low-grade metamorphic evolution of chlorite in associated metapelites and metabasites: an integrated TEM and XRD study. J Metam Geol 18:531–550

Árkai P, Fenninger A, Nagy G (2002) Effects of lithology and bulk chemistry on phyllosilicate reaction progress in the low-T metamorphic Graz Paleozoic, Eastern Alps, Austria. Eur J Mineral 14:673–686

Árkai P, Faryad SW, Vidal O, Balogh K (2003) Very low-grade metamorphism of sedimentary rocks of the Meliata unit, Western Carpathians, Slovakia: implications of phyllosilicate characteristics. Intern J Earth Sci 92:68–85

Bakker RJ (2003) Package FLUIDS 1. Computer programs for analysis of fluid inclusion data and for modelling bulk fluid properties. Chem Geol 194:3–23

Baldwin SL, Monteleone BD, Webb LE, Fitzgerald PG, Grove M, June Hill E (2004) Pliocene eclogite exhumation at plate tectonic rates in eastern Papua New Guinea. Nature 431:263–267

Berger A, Schmid SM, Engi M, Bousquet R, Wiederkehr M (2011) Mechanisms of mass and heat transport during Barrovian metamorphism: A discussion based on field evidence from the Central Alps (Switzerland/northern Italy). Tectonics 30:TC1007

Beyssac O, Goffé B, Chopin C, Rouzaud JN (2002) Raman spectra of carbonaceous material in metasediments: a new geothermometer. J Metam Geol 20:859–871

Beyssac O, Goffé B, Petitet JP, Froigneux E, Moreau M, Rouzaud JN (2003) On the characterization of disordered and heterogeneous carbonaceous materials by Raman spectroscopy. Spectrochim Acta, Part A 59:2267–2276

Bhatia MR, Crook KAW (1986) Trace element characteristics of graywackes and tectonic setting discrimination of sedimentary basins. Contrib Mineral Petrol 92:181–193

Bodnar RJ (1993) Revised equation and table for determining the freezing point depression of H_2O-NaCl solutions. Geochim Cosmochim Acta 57:683–684

Bons PD, Jessell M (1997) Experimental simulation of the formation of fibrous veins by localised dissolution-precipitation creep. Mineral Mag 61:53–63

Bousquet R, Oberhänsli R, Goffé B, Jolivet L, Vidal O (1998) High-pressure–low-temperature metamorphism and deformation in the Bündnerschiefer of the Engadine window: implications for the regional evolution of the eastern Central Alps. J Metam Geol 16:657–674

Bousquet R, Goffé B, Vidal O, Oberhänsli R, Patriat M (2002) The tectono-metamorphic history of the Valaisan domain from the Western to the central Alps: new constraints on the evolution of the Alps. Geol Soc Am Bull 114:207–225

Brantley SL, Voigt D (1989) Fluids in metamorphic rocks: effects of fluid chemistry on quartz microcrack healing. In: Miles DL (ed) Water-rock interaction. Rotterdam, Netherlands, pp 113–116

Burke EAJ (2001) Raman microspectrometry of fluid inclusions. Lithos 55:139–158

Cathelineau M (1988) Cation site occupancy in chlorites and illites as function of temperature. Clay Miner 23:471–485

Cherniak DJ (2010) Diffusion in quartz, melilite, silicate perovskite, and mullite. Rev Mineral Geochem 72:735–756

Coggon R, Holland TJB (2002) Mixing properties of phengitic micas and revised garnet-phengite thermobarometers. J Metam Geol 20:683–696

Connolly JAD, Petrini K (2002) An automated strategy for calculation of phase diagram sections and retrieval of rock properties as a function of physical conditions. Earth Planet Sci Lett 20:697–708

Cox SF, Etheridge MA (1983) Crack-seal fibre growth mechanisms and their significance in the development of oriented layer silicate microstructures. Tectonophys 92:147–170

Dale J, Powell R, White RW, Elmer FL, Holland TJB (2005) A thermodynamic model for Ca-Na clinoamphiboles in Na_2O-CaO-FeO-MgO-Al_2O_3-SiO_2-H_2O-O for petrological calculations. J Metam Geol 23:771–791

de Caritat P, Hutcheon I, Walshe JL (1993) Chlorite geothermometry; a review. Clays Clay Miner 41:219–239

Dolejs D, Wagner T (2008) Thermodynamic modeling of non-ideal mineral-fluid equilibria in the system Si–Al–Fe–Mg–Ca–Na–K–

H–O–Cl at elevated temperatures and pressures: implications for hydrothermal mass transfer in granitic rocks. Geochim Cosmochim Acta 72:526–553

Doublier MP (2010) Application of SWIR spectroscopy in very low-grade metamorphic environments: a comparison with XRD methods. In: Doublier MP, Roache A, Potel S (eds) Title. Geological Survey of Western Australia, Perth

Engi M (2011) Metamorphic structure and evolution of the Central Alps. Géochronique 117:1–11

Essene EJ, Peacor DR (1995) Clay mineral thermometry; a critical perspective. Clays Clay Miner 43:540–553

Fall A, Tattitch B, Bodnar RJ (2011) Combined microthermometric and Raman spectroscopic technique to determine the salinity of H_2O-CO_2-NaCl fluid inclusions based on clathrate melting. Geochim Cosmochim Acta 75:951–964

Ferreiro Mählmann R, Petrova TV, Pironon J (2002) Transmission electron microscopy study of carbonaceous material in a metamorphic profile from diagenesis to amphibolite facies (Bündnerschiefer, Eastern Switzerland). Schweiz Mineral Petrogr Mitt 82:253–272

Fisher DM, Brantley SL (1992) Models of quartz overgrowth and vein formation: deformation and episodic fluid flow in an ancient subduction zone. J Geophys Res 97:20043–20061

Frey M (1974) Alpine metamorphism of pelitic and marly rocks of the Central Alps. Schweiz Mineral Petrogr Mitt 54:489–506

Frey M (1986) Very low-grade metamorphism of the Alps—an introduction. Schweiz Mineral Petrogr Mitt 66:13–27

Frey M (1987a) The reaction-isograd kaolinite + quartz = pyrophyllite + H_2O, Helvetic Alps, Switzerland. Schweiz Mineral Petrogr Mitt 67:1–11

Frey M (1987b) Low temperature metamorphism. Blackie and Sons, Glasgow

Frey M (1988) Discontinuous inverse metamorphic zonation, Glarus Alps, Switzerland: evidence from illite "crystallinity" data. Schweiz Mineral Petrogr Mitt 68:171–183

Frey M, Ferreiro Mählmann R (1999) Alpine metamorphism of the Central Alps. Schweiz Mineral Petrogr Mitt 79:135–154

Frey M, Teichmüller M, Teichmüller R, Mullis J, Künzi B, Breitschmid A, Gruner U, Schwizer B (1980) Very low-grade metamorphism in external parts of the Central Alps: illite crystallinity, coal rank and fluid inclusion data. Ecl Geol Helv 73:173–203

Frezzotti ML, Tecce F, Casagli A (2012) Raman spectroscopy for fluid inclusion analysis. J Geochem Explor 112:1–20

Garofalo PS (2011) The composition of Alpine marine sediments (Bündnerschiefer Formation, W Alps) and the mobility of their chemical components during orogenic metamorphism. Lithos 128:55–72

Giggenbach WF (1988) Geothermal solute equilibria. Derivation of Na–K–Mg–Ca geoindicators. Geochim Cosmochim Acta 52:2749–2765

Goldstein RH, Reynolds TJ (1994) Systematics of fluid inclusions in diagenetic minerals. Society of Sedimentary Geology Short Course Series 31, 199 p

Goscombe BD, Passchier CW, Hand M (2004) Boudinage classification: end-member boudin types and modified boudin structures. J Struct Geol 26:739–763

Guillong M, Heinrich CA (2007) Sensitivity enhancement in laser ablation ICP-MS using small amounts of hydrogen in the carrier gas. J Anal Atom Spectrom 22:1488–1494

Guillong M, Latkoczy C, Seo JH, Günther D, Heinrich CA (2008a) Determination of sulfur in fluid inclusions by laser ablation ICP-MS. J Anal Atom Spectrom 23:1581–1589

Guillong M, Meier DL, Allan MM, Heinrich CA, Yardley BWD (2008b) SILLS: a MATLAB-based program for the reduction of laser ablation ICP-MS data of homogeneous materials and inclusions. Mineral Assoc Canada Short Course Ser 40:328–333

Günther D, Frischknecht R, Heinrich CA, Kahlert HJ (1997) Capabilities of an argon fluoride 193 nm excimer laser for laser ablation inductively coupled plasma mass spectometry microanalysis of geological materials. J Anal Atom Spectrom 12:939–944

Heinrich CA (1986) Eclogite facies regional metamorphism of hydrous mafic rocks in the Central Alpine Adula nappe. J Petrol 27:123–154

Heinrich CA, Pettke T, Halter WE, Aigner-Torres M, Audetat A, Günther D, Hattendorf B, Bleiner D, Guillong M, Horn I (2003) Quantitative multi-element analysis of minerals, fluid and melt inclusions by laser-ablation inductively-coupled-plasma mass-spectrometry. Geochim Cosmochim Acta 67:3473–3497

Holland T, Powell R (1991) A Compensated-Redlich-Kwong (CORK) equation for volumes and fugacities of CO2 and H2O in the range 1 bar to 50 kbar and 100–1600°C. Contrib Mineral Petrol 109:265–273

Holland TJB, Powell R (1998) An internally consistent thermodynamic data set for phases of petrological interest. J Metam Geol 16:309–343

Holland T, Powell R (2003) Activity-composition relations for phases in petrological calculations: an asymmetric multicomponent formulation. Contrib Mineral Petrol 145:492–501

Holland T, Baker J, Powell R (1998) Mixing properties and activity-composition and relationships of chlorites in the system MgO-FeO-Al_2O_3-SiO_2-H_2O. Eur J Mineral 10:395–406

Johnson WM, Maxwell JA (1981) Rock and mineral analysis, 2nd edn. Wiley, New York

Julien M, Goffé B (1993) Occurrences de cookeite et de pyrophyllite dans les schistes du Dauphinois (Isère, France): conséquences sur la répartition du métamorphisme dans les zones externes alpines. Schweiz Mineral Petrogr Mitt 73:357–363

Kendrick MA, Phillips D, Wallace M, Miller JML (2011) Halogens and noble gases in sedimentary formation waters and Zn-Pb deposits: a case study from the Lennard Shelf, Australia. Appl Geochem 26:2089–2100

Kharaka YK, Mariner RH (1989) Chemical geothermometers and their application to formation waters from sedimentary basins. In: Naeser ND, McCulloh TH (eds) Thermal history of sedimentary basins. Springer, New-York, pp 99–117

Kisch HJ (1991) Illite crystallinity: recommendations on sample preparation, X-ray diffraction settings, and interlaboratory samples. J Metam Geol 9:665–670

Kretz R (1983) Symbols for rock-forming minerals. Am Mineral 68:277–279

Kübler B, Jaboyedoff M (2000) Illite crystallinity. Compt Rend Earth Sci 331:75–89

Lahfid A, Beyssac O, Deville E, Negro F, Chopin C, Goffé B (2010) Evolution of the Raman spectrum of carbonaceous material in low-grade metasediments of the Glarus Alps (Switzerland). Terra Nova 22:354–360

Lanari P, Guillot S, Schwartz S, Vidal O, Tricart P, Riel N, Beyssac O (2012) Diachronous evolution of the alpine continental subduction wedge: evidence from P–T estimates in the Briançonnais Zone houillère (France – Western Alps). J Geodyn 56–57:39–54

Land LS, Macpherson GL, Mack LE (1988) The geochemistry of saline formation waters, Miocene, offshore Lousiana. Gulf Coast Assoc Geol Soc Transact 38:503–511

Laubscher HP, Bernoulli D (1982) History and deformation in the Alps. In: Hsu KJ (ed) Mountain building processes. Academic Press, London, pp 169–180

Manning CE (2004) The chemistry of subduction-zone fluids. Earth Planet Sci Lett 223:1–16

Marshall D, Pfeifer HR, Hunziker JC, Kirschner D (1998) A pressure-temperature-time path for the NE Mont-Blanc massif. Fluid-inclusion, isotopic and thermobarometric evidence. Eur J Mineral 10:1227–1240

Mazurek M (1999) Evolution of gas and aqueous fluid in low-permeability argillaceous rocks during uplift and exhumation of the central Swiss Alps. Appl Geochem 15:223–246

McCaffrey MA, Lazar B, Holland HD (1987) The evaporation path of seawater and the coprecipitation of Br^- and K^+ with halite. J Sediment Res 57:928–937

McCaig AM, Tritlla J, Banks DA (2000) Fluid mixing and recycling during Pyrenean thrusting: evidence from fluid inclusion halogen ratios. Geochim Cosmochim Acta 64:3395–3412

Merriman RJ, Frey M (1999) Patterns of very low-grade metamorphism in metapelitic rocks. In: Frey M (ed) Low temperature metamorphism. Blackwell, Glasgow, pp 61–107

Merriman RJ, Peacor DR (1999) Very low-grade metapelites: mineralogy, microfabrics and measuring reaction progress. In: Frey M (ed) Low temperature metamorphism. Blackwell, Glasgow, pp 10–60

Miron GD, Neuhoff PS, Amthauer G (2012) Low-temperature hydrothermal metamorphic mineralization of island-arc volcanics, South Apuseni Mountains, Romania. Clays Clay Miner 60:1–17

Mullis J (1975) Growth conditions of quartz crystals from Val d'Illiez (Valais, Switzerland). Schweiz Mineral Petrogr Mitt 55:419–429

Mullis J (1979) The system methane-water as a geological thermometer and barometer from the external part of the Central Alps. Bull Mineral 102:526–536

Mullis J (1987) Fluid inclusion studies during very low-grade metamorphism. In: Frey M (ed) Low temperature metamorphism. Blackwell, Glasgow, pp 162–199

Mullis J (1988) Rapid subsidence and upthrusting in the Northern Apennines, deduced by fluid inclusion studies in quartz crystals from Porretta Terme. Schweiz Mineral Petrogr Mitt 88:157–170

Mullis J (1996) P–T-t path of quartz formation in extensional veins of the Central Alps. Schweiz Mineral Petrogr Mitt 76:159–164

Mullis J, Dubessy J, Poty B, O'Neil J (1994) Fluid regimes during late stages of a continental collision: physical, chemical, and stable isotope measurements of fluid inclusions in fissure quartz from a geotraverse through the Central Alps, Switzerland. Geochim Cosmochim Acta 58:2239–2267

Mullis J, Rahn M, Schwer P, de Capitani C, Stern WB, Frey M (2002) Correlation of fluid inclusion temperatures with illite "crystallinity" data and clay mineral chemistry in sedimentary rocks from the external part of the Central Alps. Schweiz Mineral Petrogr Mitt 82:325–340

Niggli E, Niggli C (1965) Karten der Verbreitung einiger Mineralien der alpidischen Metamorphose in den Schweizer Alpen (Stilpnomelan, Al-alkali-Amphibol, Chloritoid, Staurolith, Disthen, Sillimanit). Eclogae Geol Helv 58:335–368

Oberhänsli R, Goffé B, Bousquet R (1995) Record of a HP-LT metamorphic evolution in the Valais zone: geodynamic implications. Bolletino del Museo Regionale di Scienze Naturali 13:221–240

Oliver NHS, Bons PD (2001) Mechanisms of fluid flow and fluid–rock interaction in fossil metamorphic hydrothermal systems inferred from vein–wallrock patterns, geometry and microstructure. Geofluids 1:137–162

Pettke T, Diamond LW, Kramers JD (2000) Mesothermal gold lodes in the north-western Alps: a review of genetic constraints from radiogenic isotopes. Eur J Mineral 12:213–230

Pimenta MA, Dresselhaus G, Dresselhaus MS, Cancado LG, Jorio A, Saito R (2007) Studying disorder in graphite-based systems by Raman spectroscopy. Phys Chem Chem Phys 9:1276–1290

Potter PE, Shimp NF, Witters J (1963) Trace elements in marine and fresh-water argillaceous sediments. Geochim Cosmochim Acta 27:669–694

Poty BP, Stalder HA, Weisbrod AM (1974) Fluid inclusions studies in quartz from fissures of Western and Central Alps. Schweiz Mineral Petr Mitt 54:717–752

Ramsay JG (1980) The crack-seal mechanism of rock deformation. Nature 284:135–139

Reynolds RC (1965) Geochemical behaviour of boron during the metamorphism of carbonate rocks. Geochim Cosmochim Acta 29:1101–1114

Sadezky A, Muckenhuber H, Grothe H, Niessner R, Pöschl U (2005) Raman microspectroscopy of soot and related carbonaceous materials: spectral analysis and structural information. Carbon 43:1731–1742

Saffer DM, Tobin HJ (2011) Hydrogeology and mechanics of subduction zone forearcs: fluid flow and pore pressure. Ann Rev Earth Planet Sci 39:157–186

Schmid SM, Pfiffner OA, Froitzheim N, Schönborn G, Kissling E (1996) Geophysical-geological transect and tectonic evolution of the Swiss-Italian Alps. Tectonics 15:1036–1064

Seo JH, Guillong M, Aerts M, Zajacz Z, Heinrich CA (2011) Microanalysis of S, Cl, and Br in fluid inclusions by LA-ICP-MS. Chem Geol 284:35–44

Spivack AJ, Palmer MR, Edmond JM (1987) The sedimentary cycle of the boron isotopes. Geochim Cosmochim Acta 51:1939–1949

Stampfli GM, Mosar J, Marquer D, Marchant R, Baudin T, Borel G (1998) Subduction and obduction processes in the swiss Alps. In Vauchez A Meissner R (Eds): continents and their mantle root. Tectonophysics 296:159–204

Steinmann M (1994) Die nordpenninischen Bündnerschiefer der Zentralalpen Graubündens. PhD thesis, ETH Zurich

Stoffell B, Wilkinson JJ, Jeffries TE (2004) Metal transport and deposition in hydrothermal veins revealed by 213 nm UV laser ablation microanalysis of single fluid inclusions. Am J Sci 304:533–557

Stoffell B, Appold MS, Wilkinson JJ, McClean NA, Jeffries TE (2008) Geochemistry and evolution of Mississippi Valley-Type mineralizing brines from the Tri-State and northern Arkansas districts determined by LA-ICP-MS microanalysis of fluid inclusions. Econ Geol 103:1411–1435

Tarantola A, Mullis J, Vennemann T, Dubessy J, de Capitani C (2007) Oxidation of methane at the CH_4/H_2O-(CO_2) transition zone in the external part of the Central Alps, Switzerland: evidence from stable isotope investigations. Chem Geol 237:329–357

Tarantola A, Mullis J, Guillaume D, Dubessy J, de Capitani C, Abdelmoula M (2009) Oxidation of CH_4 to CO_2 and H_2O by chloritization of detrital biotite at 270 ± 5°C in the external part of the Central Alps, Switzerland. Lithos 112:497–510

Thompson AB (1997) Flow and focusing of metamorphic fluids. In: Yardley BWD (ed) Fluid flow and transport in rocks: mechanisms and effects. Chapman and Hall, London, pp 297–314

Thompson AB (2010) Perspectives on metamorphic processes and fluids. Elements 6:142–143

Touret JLR (2001) Fluids in metamorphic rocks. Lithos 55:1–25

Trommsdorff V (1966) Progressive Metamorphose kieseliger Karbonatgesteine in den Zentralalpen zwischen Bernina und Simplon. Schweiz Mineral Petrogr Mitt 46:431–460

Vidal O, Goffé B (1991) Cookeite $LiAl_4(Si_3Al)O_{10}(OH)_8$: experimental study and thermodynamical analysis of its compatibility relations in the $Li_2O-Al_2O_3-SiO_2-H_2O$ system. Contrib Mineral Petrol 108:72–81

Wagner T, Jochum J (2002) Fluid-rock interaction processes related to hydrothermal vein-type mineralization in the Siegerland district, Germany: implications from inorganic and organic alteration patterns. Appl Geochem 17:225–243

Wang H, Frey M, Stern WB (1996) Diagenesis and metamorphism of clay minerals in the Helvetic Alps of Eastern Switzerland. Clays Clay Miner 44:96–112

Wiederkehr M, Bousquet R, Schmid SM, Berger A (2008) From subduction to collision: thermal overprint of HP/LT metasediments in the north-eastern Lepontine Dome (Swiss Alps) and consequences regarding the tectono-metamorphic evolution of the Alpine orogenic wedge. Swiss J Geosci 101:127–155

Wiederkehr M, Sudo M, Bousquet R, Berger A, Schmid SM (2009) Alpine orogenic evolution from subduction to collisional thermal overprint: the ^{40}Ar/^{39}Ar age constraints from the Valaisan Ocean, central Alps. Tectonics 28:TC6009

Wiederkehr M, Bousquet R, Ziemann M, Berger A, Schmid SM (2011) 3-D assessment of peak-metamorphic conditions by Raman spectroscopy of carbonaceous material: an example from the margin of the Lepontine dome (Swiss Central Alps). Intern J Earth Sci 100:1029–1063

Wilson AD (1960) The micro-determination of ferrous iron in silicate minerals by a volumetric and a colorimetric method. Analyst 85:823–827

Wood SA, Samson IM (1998) Solubility of ore minerals and complexation of ore metals in hydrothermal solutions. Rev Econ Geol 10:33–76

Wunder B, Meixner A, Romer RL, Wirth R, Heinrich W (2005) The geochemical cycle of boron: constraints from boron isotope partitioning experiments between mica and fluid. Lithos 84:206–216

Yardley BWD (2005) 100th Anniversary Special Paper: metal concentrations in crustal fluids and their relationship to ore formation. Econ Geol 100:613–632

Yardley BWD, Banks DA, Bottrell SH, Diamond LW (1993) Post-metamorphic gold-quartz veins from N.W. Italy: the composition and origin of the ore fluid. Mineral Mag 57:407–422

Zhang Y, Frantz JD (1987) Determination of homogenization temperature and densities of supercritical fluid in the system NaCl–KCl–$CaCl_2$–H_2O using synthetic fluid inclusions. Chem Geol 64:335–350